Nuclear Engineering and Design 392 (2022) 111769

Contents lists available at ScienceDirect

Nuclear Engineering and Design

journal homepage: www.elsevier.com/locate/nucengdes

Experiments in free falling and downward cocurrent annular flows – Characterization of liquid films and interfacial waves

Y. Rivera, C. Berna *, J.L. Muñoz-Cobo, A. Escrivá, Y. Córdova

Instituto Universitario de Ingeniería Energética, Universitat Politècnica de València (UPV), Camino de Vera 14, 46022 Valencia, Spain

ARTICLE INFO

Keywords:
Gas-liquid interface
Interfacial waves
Disturbance waves
Annular downward cocurrent flow
Conductance probe

ABSTRACT

Falling liquid films and downward cocurrent flows in rounded shape pipes have been experimentally studied during the last decades, estimating the evolution of its major characteristics. The most important variables during the formation and growth of surface waves in falling downward flows have been measured using conductance probes.

The main objective of the current research paper is to study the dependency of the characteristics of the thin liquid layer for downward cocurrent annular flows. The GEPELON experimental facility consists of a vertical pipe with 3.8 m of useful test length. Two pipe diameters have been analysed in this experimental study, 42 and 30 mm, in which the range covered by the liquid Reynolds number varies between 570 and 8500 and 800–7900 respectively, while the gas Reynolds numbers vary from 0 to $7.9{\cdot}10^4$ and from 0 to $1.1{\cdot}10^5$ respectively for the mentioned pipe diameters. Up to five conductance probes have been placed along the pipes test sections to capture the liquid film thickness fluctuations along time at different distances of the pipe entrance for both developing and fully developed regions.

After the study and analysis of the experimental data, the central point of this paper has been the development of new correlations for the liquid film thicknesses and the two major properties of the interfacial waves. Their adjustment procedure has been carried out in terms of dimensionless numbers, aiming to provide more general relationships. In particular, the magnitudes that characterise the interface behavior have been measured, particularly film thicknesses, average disturbance wave amplitudes, and disturbance wave frequencies for each boundary condition.

An additional part of the document contains an extensive comparison between the results obtained in this study and the data and expressions of other authors. It has been confirmed the significant dispersion existing among different researchers, especially when analysing variables related to the interfacial waves. This highlights the lack of knowledge in some aspects even today. The different correlations proposed have been calculated based on the best fit of the data from all the series of experiments carried out in this study. Comparisons of the behaviour of these correlations with data from other researchers have also been included.

1. Introduction

The hydrodynamic behaviour of downward cocurrent gas–liquid annular flows has been vastly investigated over the past decades due to its huge importance in a broad range of industrial and natural processes. Specifically, a wide variety of phenomena involving free falling films is found in nature. In addition, thin liquid films freely falling or helped by a gas current appear in many industrial applications. Examples of industrial applications in which cocurrent flows occur are nuclear reactors, evaporators, condensers, and distillation columns. In particular, downward flows are observed in the nuclear industry under accidental scenarios for BWR and PWR (boiling and pressurised water reactors, respectively). In PWRs, downward flows appear in LOCAs (Loss of Coolant Accidents) and LOHS (Loss of Heat Sink Accidents) scenarios. While for BWRs, this kind of flow can be shown above the core after the injection of the ECCS (Emergency Core Coolant Systems). The characteristics of the liquid film sliding on the wall determine the heat transfer coefficient. The development of surface waves at the gas–liquid interface favours eddies' appearance, increasing the heat and mass exchange. Consequently, in order to be able to enhance the design and operation of

* Corresponding author.
E-mail address: ceberes@upv.es (C. Berna).

https://doi.org/10.1016/j.nucengdes.2022.111769
Received 23 February 2021; Received in revised form 1 March 2022; Accepted 11 April 2022

all these systems, reducing costs and increasing efficiency, a better understanding of all physical processes involved in falling films is of great importance. Because of all these research studies, a considerable number of experimental investigations have shown that interfacial waves on a thin liquid film can substantially enhance the heat, momentum, and mass transfer rates.

In the early 20th century, Nusselt's research was one of the first to study the hydrodynamic characteristics of a thin laminar liquid film freely falling under the gravity effects (Nusselt, 1916a,b). Nusselt's model is the trivial solution of the conservation equations for a liquid film falling in a semi-infinite flat plate. Instead of the multiple simplifications of Nusselt's model, the calculations correctly estimate the liquid thickness under laminar conditions. In 1965, Kapitza proposed a modification of Nusselt's theoretical expression applicable for smooth wavy laminar flows (Aliyu, 2015). Many researchers have tried to obtain analytical solutions or empirical correlations to determine the major liquid layer characteristics under turbulent regime conditions. For instance, Mudawwar and El-Masri (1986) proposed a semi-empirical correlation, which has shown a good accuracy against many experimental data series, but many other empirical expressions are also available (Takahama and Kato, 1980; Brauner, 1987; Padmanaban, 2006; Aliyu, 2015).

Falling films, as they evolve downward, become turbulent and generate complex interfacial waves, which seemingly behaves randomly. This situation is favoured when cocurrent airflows are present. The wave generation and growth are dependent on the gravity force, the shear stress and the surface tension on the free gas–liquid interface. The way the surface waves emerge and grow and the hydrodynamic characteristics of the solitary waves play an essential role in the heat transfer enhancement. The initial basis which tried to understand and characterise downwards concurrent annular flows started in the 60 s and 70 s (Fulford, 1964; Telles and Dukler, 1970; Chu and Dukler, 1974, 1975).

In addition, first attempts to understand the importance of the behaviour of the huge number of tridimensional interfacial waves, which are always present in any situation in which a gas–liquid interface exists, also comes from the 60 s (Hanratty and Hershman, 1961; Hall-Taylor et al., 1963; Wallis, 1969; Hewitt and Hall-Taylor, 1970). Two major types of interfacial waves are usually recognised that coexists on the interface between the liquid and the gas, the disturbance waves (DW) and the ripple waves (RW). It is important to emphasise that a precise nomenclature and definition of these types of waves continues up to now unsettled, even though some characteristics differencing both types of waves can be given. DWs are larger than RWs and also have significantly higher lifetimes. In addition, it is widely recognised that DWs cover the entire annulus of the tube. While RWs cover the surface between DWs, along the base film region and even over the DWs. The DWs' amplitude is much higher than those of RW, being several times larger than the mean thickness of the liquid layer. RWs are considered to be not coherent. Sekoguchi speaks about a third type of interfacial waves, the ephemeral waves, described in detail in Wolf's PhD (Wolf, 1995). These waves have amplitudes and lifetimes between RWs and DWs, being not circumferentially coherent and travelling at lower velocities than DWs. Ephemeral waves appear at the rear part of DWs, travelling between two adjacent DWs, until being reached and swallowed by the next DW. A possible cause of their appearance could be droplet deposition at high liquid flow rates. A fourth type of wave was observed by Alekseenko et al., Ohba and Nagae, the so-called "ring waves" (Alekseenko et al. 2009, 2015). This type of wave was located in a narrow region near the onset of the entrainment region of upward annular flow, having characteristics quite similar to that of the ephemeral waves. Another type of wave is also mentioned by Sekoguchi (Alekseenko et al., 2015), the "huge waves". They are observed at low gas and high liquid flow rates and are associated with the transition regime between slug/churn to annular flow. Huge waves are of higher amplitude, size and velocity than the DWs.

Not only the research mentioned above have been carried out related to the characterisation of the liquid and interfacial properties of annular flows. Many other research articles over the last years (Alekseenko et al., 2008, 2009, 2014, Berna et al., 2014, 2015; Dasgupta et al., 2017; Schubring and Shedd, 2008; Setyawan et al., 2016; Belt et al., 2010) concentrate on the wavy gas–liquid interface. Some of these studies were carried out for upward flow conditions, while others were under downward flows conditions. However, all of them provide additional details and/or consolidate the ones described above.

For instance, Berna's studies displayed a review of the most widely used expressions for annular flow characterisation along with several new correlations (Berna et al., 2014, 2015). Alekseenko et al. (2014), under cocurrent downward flow conditions, explain that DWs and RWs are usually considered independently, while the authors consider that RWs' properties depend on the distance to the DWs. Three different zones are considered: the crest of DWs, the back slope of DWs and the base film zone. Fast RWs are shown in the first zone, while slow RWs exists in the base film region. The RWs are formed in the back slope of the DWs, and they gradually develop and stabilise as they move away from their creation point. The slow RWs run down the DW back slope, reaching the base film and travelling there until the next DW reaches it. Suppose they are formed beyond the separation or stagnation point (only exist when eddy motion is under the DWs hump, which means high enough turbulence). In that case, they accelerate towards the DWs front, where it disappears. The extinction is presumably caused by the gas shear stress, which leads them to disrupt into droplets or absorbed into the front part of the DW. Focusing on the fast and slow RWs, the authors explain that their velocities, when normalised by DWs' velocity, are almost constant for all the studied conditions. The number of fast RWs created by each DW was also constant at far distances from the entrance. Average lengths of DWs crests and back slopes decreased as gas velocity increased.

Whereas, under upward flow conditions, Dasgupta et al. (2017) goes a step further than 2014 Alekseenko's study in the relationship between DWs and RWs. The authors hypothesise that the presence of RWs is needed for a sustained DWs presence, giving a picture of the fully developed flow formed by a substrate of DWs above where large DWs move. In addition, the authors hypothesise that DWs propagate by catching downstream RWs and releasing new RWs into their upstream rear end. Even though Zhao's group showed that in the vicinity of the entrance, previously to the generation of DWs, the gas–liquid interface was plenty of waves with small amplitude and high frequency (Zhao et al., 2013). While Alekseenko's group found that, near the entrance, DWs are formed by multiple coalescence processes among these small high-frequency waves (Alekseenko et al., 2015). The authors also indicate that the most probably cause of these high frequency waves is the Kelvin-Helmholtz instability near the contact point between the gas stream and the liquid film. The authors, downstream the entrance, observed a similar phenomenon to that of the DWs formation, in this case for ephemeral waves formation, slow RWs behind the rear slope of the DWs coalesce to form these new waves.

The downward co-current annular regime characteristics, mainly those of the substrate and interfacial waves, allow distinguishing several different "sub-regimes" within it. Already in pioneering studies of annular flows, in particular those carried out by Webb and Hewitt (1975), four flow subregimes were identified, "ripple", "regular", "dual-wave" and "thick ripple" regimes, while recently, on Zadrazil's research a new regime has been proposed, the "disturbance wave" regime (Zadrazil et al., 2014). In the ripple regime, the completely gas–liquid interface is covered of RWs. The regular wave regime, flow regime in which the base film is covered by RWs, being crossed by DWs. The third type, the dual-wave regime, is characterised by the coexistence of DWs with two different shapes. The last regime identified by Webb and Hewitt, the thick ripple regime, in which the wave presence strongly diminishes, only sporadically large waves appear. The new regime identified by Zadrazil et al. (2014), the disturbance wave regime, which

is characterised by more frequent waves of large amplitude than in the rest of regimes, and also with high rates of entrainment between both phases, from gas to liquid and from liquid to gas phases.

Another important aspect that has been extensively treated over the last decades are the lengths needed to reach fully developed flow. There is a conflict to determine the length needed to reach fully developed flow. Different researchers predict different development lengths depending on the analysed parameter. Usually, mean film thickness is the first variable to be fully developed, followed by wave amplitudes and finally wave frequencies. For the mean film thickness in annular flow, several researchers found that the necessary length for the flow to be fully developed depends on Re_L. Specifically, for relatively low liquid Reynolds numbers, $Re_L = 400$, the development length was found to be 32 D from the inlet. In contrast, for high liquid Reynolds numbers, $Re_l = 1000$, this length is 12D (Takahama and Kato, 1980). Other researchers explain that the wavy flow probably would not be fully developed at these distances from the flow entrance. However, changes are not as large as those for smaller distances (Karapantsios and Karabelas, 1995). For wave amplitude and frequency, distances of at least 160 and 470 D from the inlet respectively are found to be necessary to be under fully developed flow conditions (Webb and Hewitt, 1975). Even though Webb and Hewitt also report that at about 150D from the inlet, the mean wave frequency approaches its fully developed value within approximately 10% for falling films, a value that depends on the liquid Reynolds number.

Concerning the measurement techniques used to characterise the liquid film thickness, four large groups could be established (Clark, 2001), i.e., film average (hold-up measurements, weighing methods, etc.), localised (capacitance and conductance probes, etc.), point (laser scattering methods, interferometric methods, etc.) and spatial (fluorescent imaging methods, ultrasonic transmission methods, etc.). Even though electrical methods based on conductance or capacitance have been the most widely used (Cuadros et al., 2019; Dasgupta et al., 2017; Wolf et al., 2001; Belt et al., 2010). During the last years, visualisation techniques, mainly Laser-Induce Fluorescence (LIF), are also widely used (Liu et al., 2006; Schubring et al., 2010; Zadrazil et al. 2014; Alekseenko et al., 2014; Charogiannis et al., 2019). The current study is based on the variation of water conductance with film thickness, i.e., a localised method implemented using conductance probes. Specifically, five of them have been placed at different positions from the flow entrance in the current study to characterise fully developed downward flows and under development flows.

2. Experimental facility layout

2.1. The GEPELON experimental facility

The GEPELON (GEneración de PELícula ONdulatoria or translated to english Ondulatory Film Generation) experimental flow facility, at this first stage, has been designed to generate a film of liquid stuck to the wall while having the air mass in the central part, either quiescent or in co-current, i.e. downward annular air–liquid flow descending a vertical pipe. The expected phenomena will be similar to the behaviour of passive cooling systems in third-generation reactors, but only in their hydraulic behaviour. The installation does not use heated fluids; therefore, it does not take into account heat transfers between the fluids or the wall in this first stage.

The facility configurations are displayed in Fig. 1 and have been previously summarised by Rivera et al., (2020). The useful height of the experimental test section is 3.8 m approximately, and there are two different test sections, consisting of two pipes with 30 mm and 42 mm internal diameter respectively. Two main circuits constitute the facility so both air and water properties can be checked separately before being introduced into the test section. Therefore, the following main groups of components constitute the installation: the air pumping system, the water pumping system, the injection/mixing system, the test section and the water collection/recirculation system. This set of components is equipped with various devices and sensors, thus being able to measure and/or control the main variables necessary to know/modify the experimental conditions and to be able to perform the subsequent analysis.

The water used in all experimental data sets is thoroughly handled before being fed into the loop. Its properties are adequately controlled to

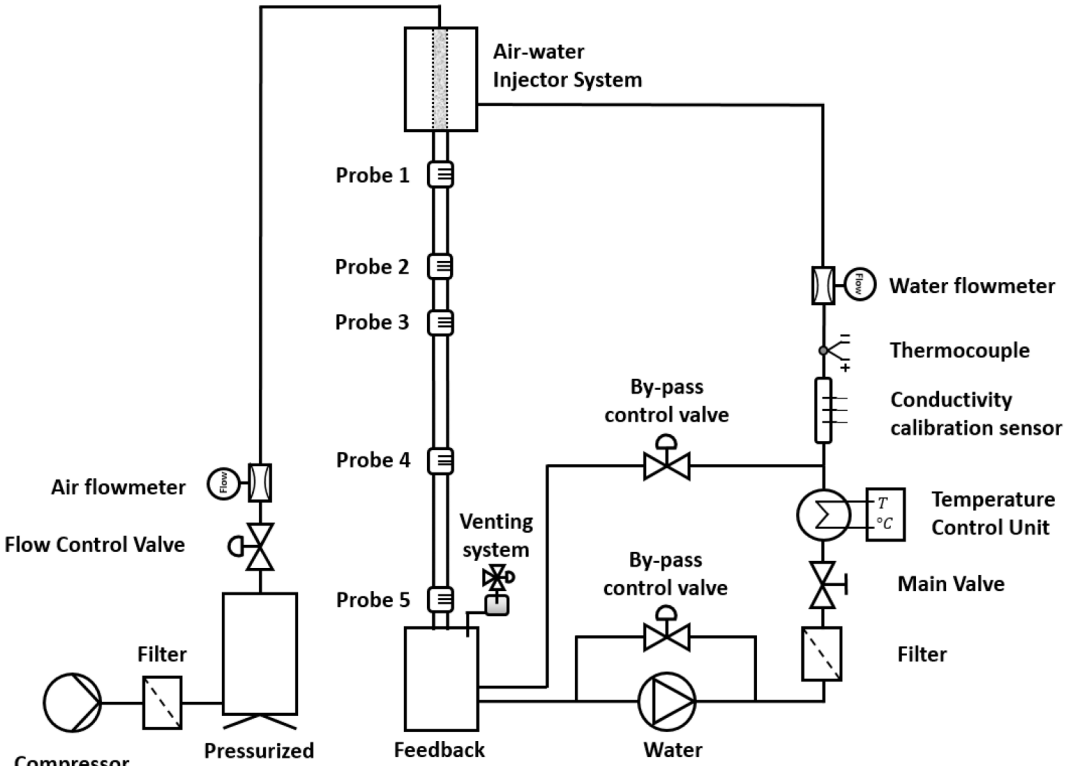

Fig. 1. Schematic view of the GEPELON flow diagram showing the five conductance probes (Rivera et al., 2020).

have an appropriate conductivity with no pollutants or impurities. Along the way from the tank to the injector, the water goes through several devices for both control and measurement. In particular, the conductivity calibration sensor, shown in Fig. 1, records any possible change in the water conductivity before the measurements are made. These measurements are sent to the data acquisition program (DAQ) to adjust the calibration curve of the different probes. However, due to the low variability of the temperature achieved by the temperature control unit, the conductivity hardly changes once such stable conditions are attained. In addition, the pump power is maintained at the correct duty point by an inverter that monitors the water flow rate and modifies the pump frequency using a PID regulator. The water temperature is also maintained in the circuit at 21 °C through a temperature control station, which changes the water temperature if necessary to keep it constant. Several regulation and safety valves, filters and other devices, as displayed in Fig. 1, are installed along the circuit for different complementary purposes.

In the free-fall configuration, the water flow is impelled into the system by a water pump (maximum pumping pressure of approximately 4.2 bar). The pump drives the water to the top of the standpipe through a self-designed pressurised water injection system. The injector's operation principle is based on the pressure difference between both sides of the device. Due to this pressure difference, the water passes through a sintered stainless steel tube (Cuadros et al., 2019). The pore size of this component is $19{\cdot}10^{-6}m$ and the coefficient of viscous permeability, y_S, is $0.8{\cdot}10^{-12}$. The injection system, the test section and the separation tank (Fig. 1) are duplicated so that there are two test sections of 42 mm and 30 mm inner diameter, both with a length of 3.8 m.

By gravity, the water descends sticking to the inner surface of the methacrylate tube and flows down through the test section, finally the water is collected in a storage tank. This water reservoir is a large capacity plastic tank, from which the water recirculation pump sucks the fluid and pushes it back into the injector system so the water starts a new loop.

The arrangement of the experimental installation for the second configuration, cocurrent experiments, is the same as the free falling with the only difference of the existence of an air injection system. The air stream is filtered, dedusted and demisted prior to its injection into the upper part of the facility, Fig. 1. The air circuit is composed of a compressor, a stabilisation tank, a flowmeter, and several safety and control valves. The compressor has a maximum working pressure of 8 bars and a maximum volumetric flow rate of 3750 l/min approximately. Even though only air flows up to 2500 l/min have been reached for the current experimental conditions.

As mentioned above, the test section consists of two vertical methacrylate tubes almost 4 m long. In the current experimental study, two different tubes have been used, one with an inner diameter of 42 mm and the other with 30 mm. Between the water injection and extraction systems, the facility has a height of approximately 5 m. The experimental conditions are measured along this test section. At five distances from the water flow entrance, interfacial wave measurement ports have been installed (labelled as Probes in Fig. 1) in order to capture the major film and wave properties.

2.2. Conductance probe

Conductance probes are based on the difference in the conductivity of the device with the thickness of the liquid film (Clark, 2001; Tiwari et al., 2014; Muñoz-Cobo et al., 2017). This technique is probably the most widely used when trying to measure temporal variations of film thicknesses. The performance of conductance probes follows the potential field theory in such a way that the behaviour of the liquid layer between electrodes subjected to an alternating current is resistive when the frequency of the excitation signal is sufficiently high (Muñoz-Cobo et al., 2020). In summary, there is a proportionality between the liquid layer between electrodes and the current transmitted between them. The conductance probe consists of three electrodes embedded in the wall and aligned parallel to the flow direction. The transmitting electrode is located at one end of the device emits a sinusoidal signal of 100 kHz and 5 Vpp. The conductance probe has a ground connection, which is placed in the central section. At the other end of the device, the receiver electrode is positioned. This electrode is responsible for the reception of the signal. The way the device works is as follows: the electrical signal is emitted by the first electrode, this signal is transmitted through the thin layer of water, and collected by the receiver so that there is a proportionality between the received signal and the liquid layer thickness.

2.2.1. Architecture of the conductance probe

All conductance probes have been built in Acrylonitrile Butadiene Styrene (ABS), this choice is justified by its excellent mechanical properties. The port design has an inside diameter equal to that of the test pipe cross-section and an overall length of approximately 170 mm. Each conductance probe has three 1.5 mm ID electrodes, each spaced 1.5 mm and aligned with the flow direction. The selection of the electrode diameter and their distance is the result of a compromise solution between the desired measurement range and the desired achievable precision of the measurements. Larger and more separated electrodes make it possible to measure larger thicknesses, which leads to lower spatial resolution measurements since they are obtained by averaging over longer lengths (Rivera et al., 2021). The stainless steel electrodes are placed in the middle section of the device. (Fig. 2A). The conductance probes are positioned near the lower part of the test section, specifically at 83 and 117 diameters of the test entrance for the 42 and 30 mm pipes respectively, as displayed in Fig. 2B.

2.2.2. Electronics of the conductance probe

A schematic view of the electronic circuit connected to the conductance probes is displayed in Fig. 3. This device has been designed to emit, receive, amplify and filter an electric signal. It consists of four high-frequency amplifiers, a couple of precision resistors (0.1% tolerance) and 1 N4148 diodes. High precision and low tolerance components have been used to make the device as accurate as possible. The electronic second-order low-pass filter is designed to cut-off frequencies above 149 Hz using the Sallen-Key architecture (Leven, 2007). Butterworth filter was selected, so the attenuation above the cut-off is −20 dB/decade.

The electronic circuit consists of two distinct parts, the transmitter and the receiver. One part of the electronic circuit generates and transmits a sine wave signal. The signal is produced by a signal generator and is directed to the electrode through the circuit that excites the transmitting electrode. While another part of the electronics picks up the signal returning from the receiving electrode, this signal will depend on the thickness of the water film between the two electrodes. Finally, the wave passes through a rectifier circuit and a filter to obtain a DC signal. This value is collected through a data acquisition card and stored in the computer for further post-processing.

The units of the initial registered raw signal are volts, values that do not directly provide any useful information, thus it is necessary to calibrate the probes beforehand to transform this raw signal (in volts) to a processed signal (in millimetres) to determine film thickness, wave amplitudes, etc. A new gadget has been designed to perform the calibration, the probe calibration device.

2.2.3. Conductance probes calibration procedure

The calibration procedure of each conductance probe must be carried out previously to their installation in the GEPELON facility. The objective of the calibration procedure is to be able to accurately correlate the voltage signal measured with the probes to the thicknesses of the water layer.

To achieve higher accuracy than in former surveys (Rivera et al., 2019; Cuadros et al., 2019), an improved device has been used, in line

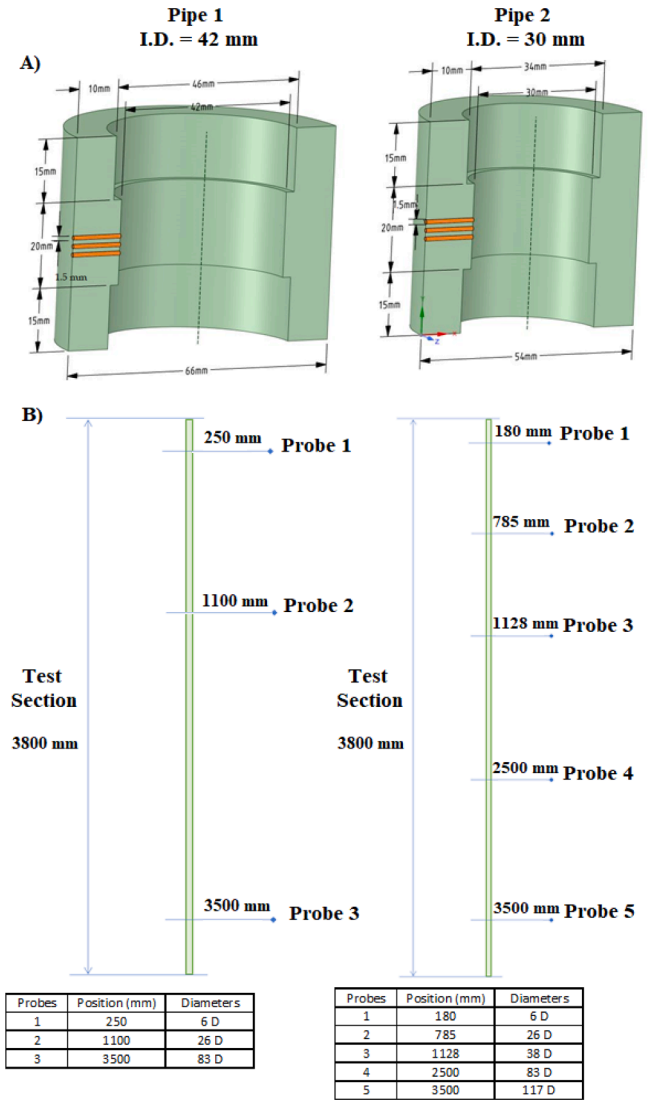

Probes	Position (mm)	Diameters
1	250	6 D
2	1100	26 D
3	3500	83 D

Probes	Position (mm)	Diameters
1	180	6 D
2	785	26 D
3	1128	38 D
4	2500	83 D
5	3500	117 D

Fig. 2. Schematic view of the conductance probes: A) Probe Geometry; B) Facility Positioning.

with the calibration gadget shown for a vertical upward facility (Rivera et al., 2021). The major components of the conductance probe calibration device are displayed in Fig. 4. The water used in the experiments has been treated to have a fluid with a controlled conductivity value. In our case, it has been set to 50μS. Multiple measurements were conducted in order to determine the optimum excitation values of the conductance probes, both for frequency and voltage. As presented above, the final excitation signal selected was a sinusoidal signal of 100 kHz and 5 Vpp.

The calibration procedure is performed on the calibration device for all conductance probes employed in the experimental sets. This gadget consists essentially of the following main parts: an electronic precision positioning system, a flatness table, and several cylinders. Each dielectric cylinder of known diameter is located through the positioning system at the central position of the interior side of the conductance probe port. A high precision positioning system allows for knowing the exact placement of the cylinders so that the exterior side of the cylinder and the interior side of the probe are at a constant known distance in their entire circumference. The existing gap between the conductance probe and the dielectric cylinder is filled with the treated water.

The major steps of the calibration procedure are as follows:

- Signal generator sends the sinusoidal signal
- Probe-emitting electrode is excited by this signal
- Electric signal goes through the know liquid layer
- The probe-receiver electrode receives attenuated signal
- The data acquisition card collects signal
- Relation between liquid layer thickness and the electric signal can be determined, as the liquid layer is known, and the signal has been measured.

The procedure has been repeated using all dielectric cylinders, in order to have enough adjustment points between electric signal and liquid layer thickness, and for each conductance probe. More than 20 calibration points have been measured for each of the 8 probes to determine any of the calibration curves.

Because of the high sensitivity to the physical properties of the environment of this type of sensors, not only the conductivity of the water but also its temperature might be of extreme importance to accurately relate the measured voltage signal to the thicknesses of the water film. Although, the shape of the calibration curve would not change appreciably due to narrow variation ranges of fluid properties affecting conductivity. Fig. 5 shows the calibration points measured with the calibration device and the fitted calibration curves for one of the probes mounted in each of the two pipes used in the experimental facility.

Additionally, in order to adjust these possible conductivity changes, a conductivity calibration sensor has been placed in the GEPELON facility, also shown in Fig. 1. This device measures the water saturation voltage and sends the value to the DAQ program to adjust the calibration curve of the different probes. Before performing the probe measurements, the conductivity calibration sensor will register any change in the

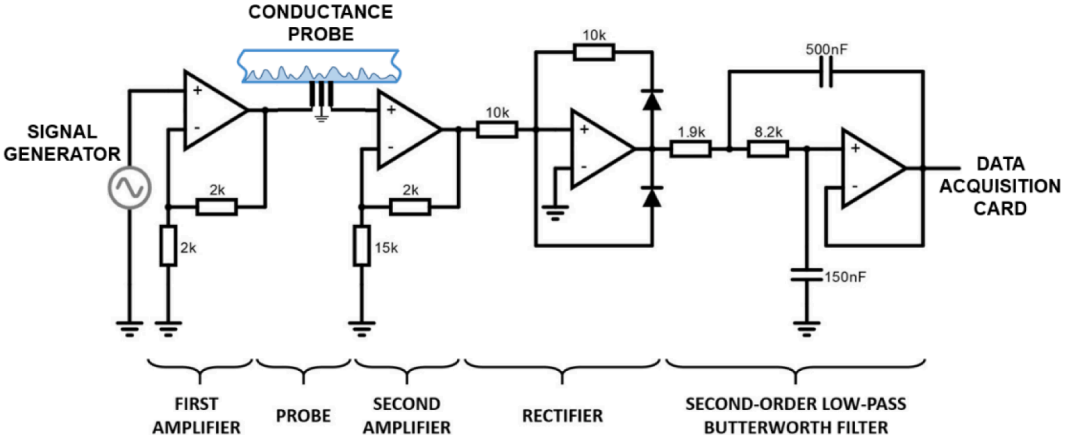

Fig. 3. Detail view of the Electronic circuit designed for the use of the conductance probe.

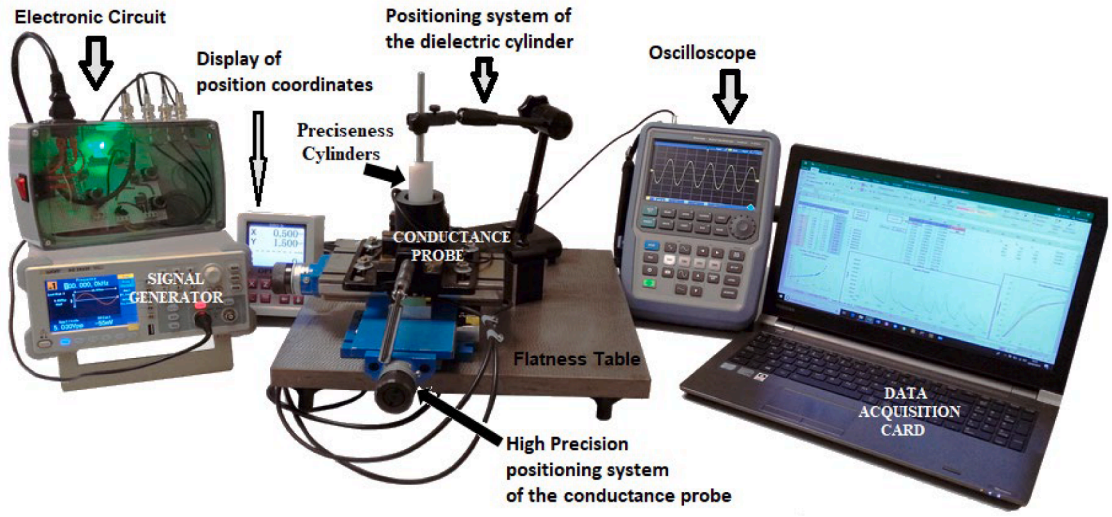

Fig. 4. Devices of the Conductance Probe Calibration Procedure.

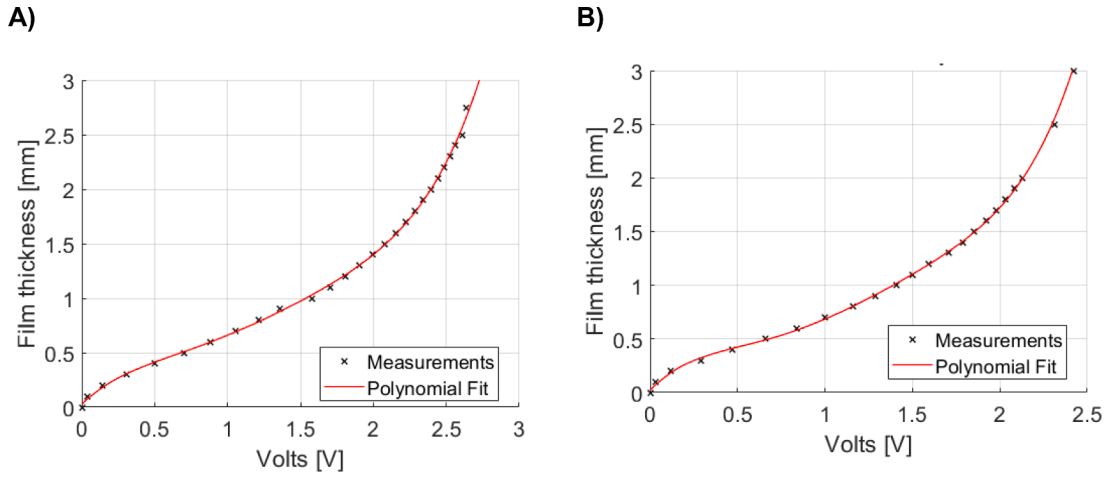

Fig. 5. Fitting Curve and Calibration Points of the Conductance Probes up to its saturation point: A) 30 mm I.D.; B) 42 mm I.D.

water conductivity. However, the conductivity does not change once stable conditions are attained due to the high temperature stability achieved with the temperature control unit.

The values for both the signal amplitudes (Volts) and their conversion in film thicknesses (mm) were smaller than 3 Volts and 3 mm respectively, as shown in Fig. 5. With this data, the calibration curves for both conductance probes, the ones for the 30 and 42 mm of inner diameter, are displayed:

$$h = 0.111\,V^5 - 0.6598\,V^4 + 1.5582\,V^3 - 1.6682V^2 + 1.2919\,V + 0.0275 \quad (1)$$

$$h = 0.299V^5 - 1.6616V^4 + 3.5121V^3 - 3.2032V^2 + 1.7184V + 0.0201 \quad (2)$$

in which V is given in Volts, and thicknesses of the liquid layer are given in mm. The determination coefficients of all polynomial fits were $R^2 = 0.9993$ and 0.9995 respectively, being the RMS errors of 0.026 and 0.0018 mm.

The expression used to calculate the fitting errors $\varepsilon_{fit,cal}$ of Eqs. (1) and (2) is found in chapter 7 of the book of Bevington and Robinson (2003) and is given by:

$$\varepsilon_{fit,cal} = \sqrt{\frac{\sum_{j=1}^{n} \left(h_i - h_{i,fit}\right)^2}{n - m}} \quad (3)$$

in which h_i are the experimental data, $h_{i,fit}$ are the values obtained using the calibration curves, n is the number of the calibration data points and m the degrees of freedom (in this case 5 polynomial degree). Carrying out the calculations for both pipes, the final values of the calibration errors are 0.026 and 0.018 mm for the 30 and 42 inner pipe diameters, respectively.

3. Experimental conditions, filtering procedure and error analysis of the conductance probe measurements

3.1. Experimental conditions test matrix

The test matrix consisted of two groups of test runs, one for each pipe diameter, changing the water and gas flows. The water flow ranges approximately from 1 to 15 and 1 to 10 l/min for the 42 and 30 mm of inner pipe diameters respectively, increasing the liquid flow rate litre by litre from the minimum value up to the maximum. In contrast, the air flow rate varies from stagnant conditions up to approximately 2500 l/min. The combinations of these two flows, both liquid and gas, have been carried out during the experimental measurement procedure. The test conditions in terms of volumetric mass flow rate, superficial velocities and superficial Reynolds numbers for the gas and liquid phases for both pipe diameters are summarised in Table 1. These dimensionless

Table 1
Experimental test matrix performed in the GEPELON facility.

Water setup range					AIR setup range				
Q_L [l/min]	J_{L_42mm} [m/s]	Re_{L_42mm}	J_{L_30mm} [m/s]	Re_{L_30mm}	Q_g [l/min]	J_{g_42mm} [m/s]	Re_{G_42mm}	J_{g_30mm} [m/s]	Re_{G_30mm}
1	0.01	560	0.02	800	0	0	0	0	0
2	0.02	1100	0.05	1600	250	3.0	7900	5.9	11,000
3	0.04	1700	0.07	2400	375	4.5	12,000	8.8	17,000
4	0.05	2300	0.09	3200	500	6.0	16,000	11.8	22,000
5	0.06	2800	0.12	4000	625	7.5	20,000	14.7	28,000
6	0.07	3400	0.14	4800	750	9.0	24,000	17.7	33,000
7	0.08	4000	0.17	5600	875	10.5	28,000	20.6	39,000
8	0.10	4500	0.19	6300	1000	12.0	32,000	23.6	44,000
9	0.11	5100	0.21	7100	1500	18.0	47,000	35.4	66,000
10	0.12	5700	0.24	8000	2000	24.1	63,000	47.2	88,000
11	0.13	6200			2500	30.1	79,000	58.9	111,000
12	0.14	6800							
13	0.16	7400							
14	0.17	7900							
15	0.18	8500							

numbers have been defined in the usual way, the gas and liquid Reynolds numbers at the fluid entrance conditions have been defined in terms of superficial velocities:

$$Re_L = \frac{\rho_l J_L D}{\mu_l} = \frac{4\ \rho_l\ Q}{\pi\ D\ \mu_l} \tag{4}$$

$$Re_G = \frac{\rho_g J_g D}{\mu_g} \tag{5}$$

In short, the theoretical ranges covered by the gas Reynolds (Re_G) are from 0 to 78,946 and from 0 − 110,524 for the 42 and 30 mm of inner diameter pipes. While the ranges covered by the liquid Reynolds (Re_L) are from 570 to 8500 and from 800 to 7900 approximately for the 42 and 30 mm of inner diameter pipes. In practice, the experimental points are not precisely those of Table 1 but those obtained from the averaged flow values for the six experimental data series for each condition.

In each test, the experimental conditions were monitored and stored in real-time. The variables acquired include volumetric water flow rates, temperatures and pressures, along with measurements from all conductance probes. The data acquisition system has been programmed in LabView software. Two forms of data acquisition are clearly differentiated according to their relevance. The main focus of the present research study is the measurements of the conductance probes. For this purpose, a PCI 6255 card from National Instruments (with 80 analogue channels and a maximum storage capacity of 1.25 MS/s) was used. This data acquisition card is capable of recording up to 10^5 samples per second. While the rest of the measurements, those of lesser importance, are collected with an acquisition system that is capable of recording 100 samples per second (National Instruments cDAQ-9174 chassis compactDAQ with a NI 9207 module with 16 analogue channels and a maximum rate of 500 S/s).

The procedure carried out for each test is as follows:

- Adjustment of the liquid flow rate to the target value.
- Verification of the stability of the main experimental parameters (temperatures, pressures, liquid flow rate), carried out by monitoring the signals in real time using the LabView program.
- Data collection, recording of two data files for ten seconds (a file with $5{\cdot}10^4$ points for the conductance probe and another file for the rest of the data with 10^3 points for each variable).

Six runs of ten seconds for each water flow rate have been carried out. Consequently, six series of $5{\cdot}10^4$ points of raw data for the conductance probe in each experimental condition have been recorded.

3.2. Measurements and errors of conductance probes

After collecting the raw data of the probe signal, the next step was to use the calibration functions. In this way, the volts versus time collected signal was converted in millimetres vs time. These signals give the liquid layer thickness evolution over time on the measurement region.

The next stage was to filter the converted raw data using a Savitzky-Golay moving average filter. The use of this type of filter is motivated by the fact that it maintains the height and width of the peaks and, in addition, causes very low distortion in the signal (Rivera et al., 2021). The Savitzky-Golay filter was applied using a polynomial of order p = 8 and a frame length of m = 101. The comparison of the film thickness signal before and after the filtering procedure using the Savitzky-Golay moving average filter shows no appreciable differences, the height and widths of the peaks remain practically unchanged after performing the Savitzky-Golay filtering procedure. However, a noticeable reduction in electronic noise has been achieved.

As a first contact to the experimental measurements, a zoom of one second for several representative gas and liquid experimental conditions for the fully developed flow (lower probe) are shown in Fig. 6. As displayed in the figure, the height of the DWs presents an appreciable decrease with the gas Reynolds number, while, at first glance, a less significant increase with the liquid Reynolds number is revealed.

The total error can be calculated by adding up the systematic and random errors in a quadratic form:

$$\boldsymbol{\varepsilon}_{total} = \sqrt{\boldsymbol{\varepsilon}_{syst}{}^2 + \boldsymbol{\varepsilon}_{acc}{}^2} \tag{6}$$

The systematical error has the following contributions: the error of the data acquisition system, i.e., the error of the voltage measurement equipment, ε_{DAQ}; the fitting error, $\varepsilon_{fit,cal}$, given by Eq. (3); and the position error during the calibration process, ε_{pos}. Then, the total value of all three terms of the systematic error can also be obtained by adding them up in a quadratic form:

$$\boldsymbol{\varepsilon}_{syst} = \sqrt{\boldsymbol{\varepsilon}_{DAQ}^2 + \boldsymbol{\varepsilon}_{fit,cal}^2 + \boldsymbol{\varepsilon}_{pos}^2} \tag{7}$$

To calculate the error caused by the data acquisition system, a propagation of the voltage error should be done in the polynomial calibration functions, given by Eqs. (1) and (2):

$$h = c_1{\cdot}V^5 + c_2{\cdot}V^4 + c_3{\cdot}V^3 + c_4{\cdot}V^2 + c_5{\cdot}V + c_6 \tag{8}$$

then, propagating the voltage errors in the previous expression:

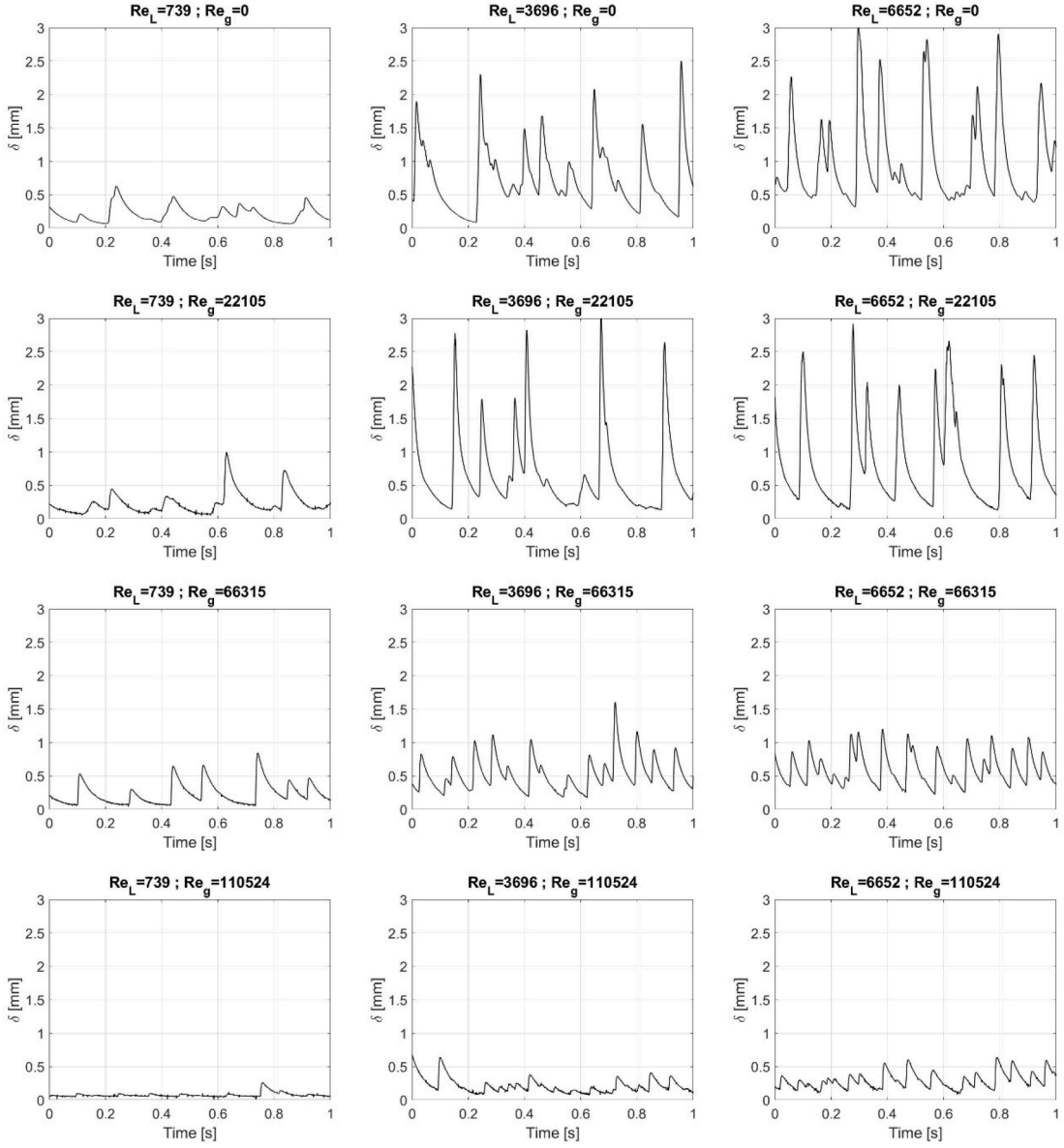

Fig. 6. One second zoom of the film thickness variation for several air–water conditions in the fully developed region for the 30 mm inner diameter pipe.

$$\varepsilon_{DAQ} = \left\{\frac{\partial f(V)}{\partial V}\right\}\varepsilon_V = \left|c_1 \cdot V^5\right| \cdot \left(5 \cdot \frac{\varepsilon_V}{V}\right) + \left|c_2 \cdot V^4\right| \cdot \left(4 \cdot \frac{\varepsilon_V}{V}\right) + \left|c_3 \cdot V^3\right| \cdot \left(3 \cdot \frac{\varepsilon_V}{V}\right) + \left|c_4 \cdot V^2\right| \cdot \left(2 \cdot \frac{\varepsilon_V}{V}\right) + \left|c_5 \cdot V\right| \cdot \sqrt{\left(\frac{\varepsilon_V}{V}\right)^2} \quad (9)$$

being the final values of the data acquisition system errors 0.0099 and 0.0155 mm for the 30 and 42 inner pipe diameters respectively.

The calibration probe positional system has a resolution of 0.002 mm, so this value has been taken as the positioning error, $\varepsilon_{pos} = 0.002mm$.

The accidental or random error (ε_{acc}) is evaluated from 6 sets (N = 6) of 10-second measurements (5000 samples/second) by means of the *Standard Error of the Mean* (½ of the confidence interval). A Matlab script processes measurement data and the random error is calculated for each test. Then, the accidental error is given by:

$$\varepsilon_{acc} = t_{n-1}^{\alpha/2}\frac{s_n}{\sqrt{n}} \quad (10)$$

being $t_{n-1}^{\alpha/2}$ the t-Student of 1-α/2 quantile for $n-1$ degrees of freedom, n the number of measurements performed, and s the quasi-variance $s_n = \sqrt{\frac{\sum (x_i - \bar{x})^2}{(N-1)}}$. The quantile value of the t-Student depends on the degrees of freedom and confidence level, having a value of 2.571 for five degrees of freedom and the widely used 95% confidence level (α = 0.05).

Finally, a summary table of the total errors for the variables estimated along this research, using Eq. (6), is displayed in Table 2.

Comment that another possible source of errors not directly attributable to the measurement procedure could be the extent of DWs

Table 2
Average error and maximum error obtained for the set of all the measurements made for this study.

Variable	Acronym	Average error	Maximum error
Mean film thickness (mm)	h_{mean}	0.020	0.025
Disturbance waves height (mm)	h_{DW}	0.059	0.155
Disturbance waves frequency (Hz)	ν_{DW}	0.418	2.85

incoherence along the circumferential section of the pipe (Cuadros et al., 2019). Summary conclusions could be that pipes of larger diameters conduct to higher DWs incoherence. In contrast, high gas flow rates lead to lower incoherence of the DWs, with no appreciable effect of the liquid mass flow rate. Anyway, as the current experimental measurements were registered during long-term intervals, then a significant mean value of the evolution of the different variables is obtained under fully developed flow conditions. Therefore, all these circumferential effects are not considered a major cause of errors.

Another source of error attributable to conductivity probes, and intrinsically unavoidable to them by their nature, is the averaging of measurements over a small region of space. As previously mentioned, to reduce this error, a compromise must be reached in the design of the probes (number and arrangement of the electrodes, as well as the distance between them and their thickness). So that the probe does not saturate before the maximum value of liquid layer to be measured but, at the same time, it is as accurate as possible. Consequently, with an appropriate design specific to the experimental conditions, it is considered that this method has acceptable precision. Different researchers (Clark, 2001; Setyawan et al., 2016; Dasgupta et al., 2017; Muñoz-Cobo et al. 2020) share this opinion. In the current case, a study of different probe configurations of probe has been carried out considering the arrangement, distance and thickness of electrodes. So that different arrangements have been analysed, for example, once the optimal thickness and distance is selected, several tests have been made with three electrode arrangements, parallel to the flow, perpendicular to the flow and forming an equilateral triangle. Although they all provide very similar measurements, probes with a flow-parallel arrangement have been used in this study. To obtain global information from a wider region and to go into more details of waveform analysis, especially of ripple waves, optical methods would probably be more suitable. Although, these methods also have drawbacks, mainly due to errors caused by total internal reflection (TIR) by refraction or TIR of fluorescence emission at the gas–liquid interface. Nevertheless, research is currently in progress to reduce these errors with very promising results (Cherdansev et al., 2019; Charogiannis et al., 2019).

4. Magnitude estimation from the conductance probe measurements

This section displays a summary of the treated measurements of the conductance probe signals, already converted into length units. Specifically, the test matrix displayed in Table 1 has been studied. Six series of 10 s for each experimental condition have been collected, from which the principal variables concerning film thickness and interfacial waves have already been analysed and estimated.

The magnitudes that have been analysed in the experiments (Fig. 7), along with their definition, are:

- Mean Film Thickness, h_{mean}, averaged value of the liquid layer thickness;
- Disturbance Wave Peak Height, h_{DW}, which is measured from pipe wall to wave crest;
- Disturbance wave frequency, v_{DW}, averaged value of the number of peaks per second.

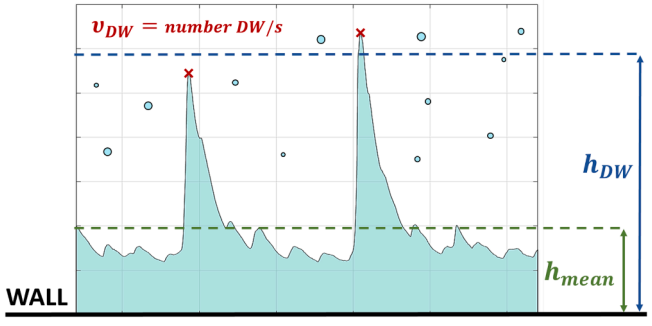

Fig. 7. Schematic representation of the major variables that determine interfacial waves properties in vertical downward concurrent flows.

4.1. Analysis of flow development with distance

Several conductance probes have been placed along the facility to study the film thickness for developed conditions and for developing flow (Fig. 1). The study of this evolution can be important because similar conditions of current research take place in different industrial processes under accidental or working conditions. For instance, both free and forced downward cocurrent flows can occur under accidental conditions on the U-tubes of steam generators in PWRs.

Fig. 9a and b show several examples of the mean film thickness variation as a function of the distance to the 30 mm inner diameter pipe entrance. As clearly shown in the figure, there is an asymptotical increase with the distance to the entrance towards a maximum value of film thickness. The value of this maximum depends on both fluid flow rates. This maximum for developed flow conditions increases with the increase of the liquid flow and decreases with the increase of the gas flow.

The evolution of the disturbance wave height with distance from the inlet follows a similar but more pronounced behavior than the mean films thickness (Fig. 8c and d). For gas Reynolds numbers lower than 44000, we observe that the height grows to probe 4, located at 83D and stabilises. The growth is much less noticeable for higher Reynolds numbers, and the variation from 26D onwards tends to stabilise. For larger gas Reynolds numbers, the thickness is minimal. The thickness of the film and its waves adopt values closer to the error, which stays around the same order of magnitude. This results in a reduction of stabilisation observed at large airflow rates.

The frequency of the disturbance waves follows a different behaviour from the other variables. Fig. 8e and f show a non-constant growth until the asymptotic zone is reached. The frequency in the first probe located at 6D from the input is very low but grows suddenly until the second probe at 26D. This may be produced by the appearance of the first interfacial waves, where the differentiation between large and small waves has not yet occurred. The wave peak calculation algorithm detects a high density of relatively small-height waves. Only a part of these waves grows, and many of them end up as part of the large waves. From this point, the frequency decreases for low gas Reynolds numbers until the last probe. For higher gas Reynolds numbers, the frequency decreases and progressively starts to increase again. In this case, the influence of the gas stream is stronger, and it is maybe the cause of the slight increase in frequency downstream.

The trend followed by the measurements is asymptotic and within what is expected to be observed. Although there are still slight differences between the measurements at 83D and 117D, it should be noted that these measurement zones are not particularly close to each other but differ by 34D. Although the flow approximates to developed conditions, it should be noted that the values obtained in an even longer pipeline might differ slightly.

4.2. Liquid film thickness measurements

Along this section, several samples of the measurements of the liquid film thicknesses through the conductance probes of both pipe diameters will be shown. In particular, the mean liquid film thickness for developed flow conditions have been estimated (h_{mean}). This variable is usually defined as the averaged distance between the pipe wall and the gas–liquid interface. The different inlet conditions, displayed in Table 1, will be compared to demonstrate its effect on the variation of this variable over time.

As could be intuitively thought-out, there should exist an increasing

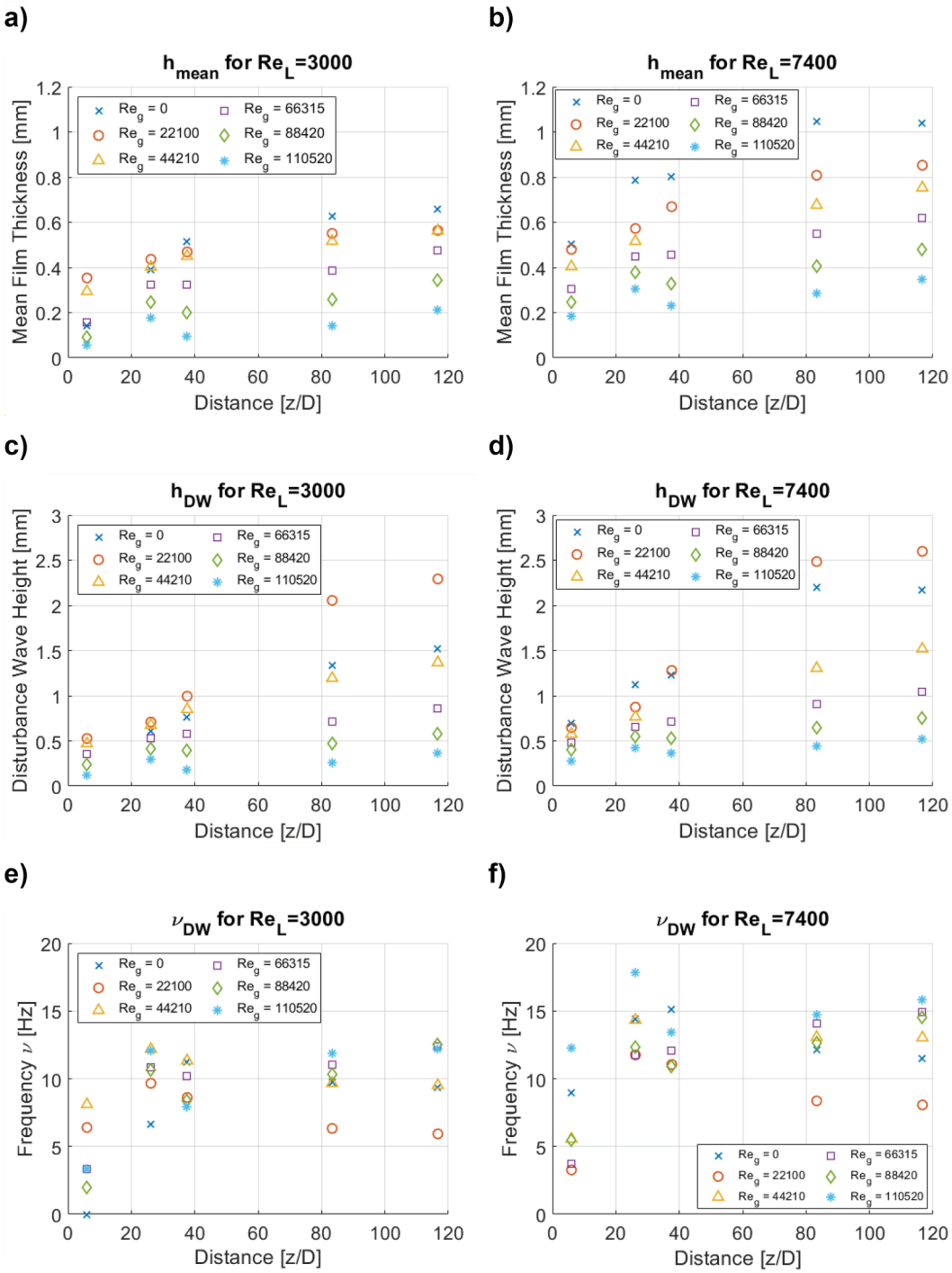

Fig. 8. Mean Film Thickness (h_{mean}) and disturbance waves height and frequency (h_{DW} and ν_{DW}) versus entrance distance for several gas Reynolds numbers at constant liquid Reynolds number: a), c), e) ReL = 3000; b), d), f) ReL = 7400.

tendency of liquid film thicknesses with the rise of water flows. While, for the gas flow rate, there should exist a decreasing tendency with the increase of the flow. In Fig. 9, examples of the evolution of the average thickness of the liquid layer for the 30 mm inner diameter pipe. Fig. 9a shows the tendency of this averaged film thickness as a function of the liquid flow rate for the different gas Reynolds numbers analysed. In contrast, Fig. 9b presents the evolution of the mean film thickness versus the gas flow rate for the different liquid Reynolds numbers. These measurements confirm that the mean film thickness diminishes with the gas flow increase. Moreover, there is also a pronounced tendency for the mean film thickness to increase when the liquid flow rises. Fig. 9c shows this thickness for both 30 and 42 mm facilities. The comparison should be made with caution as the Reynolds numbers represented with the same symbol do not correspond exactly for both diametres. The trend observed is very similar for both installations, with slight discrepancies for the high gas Reynolds number.

4.3. Measurements of the disturbance waves

Concerning the DWs, two important variables are usually considered when analysing the gas–liquid interface, the wave amplitudes and frequencies. An iterative multi-criteria procedure has been used to predict

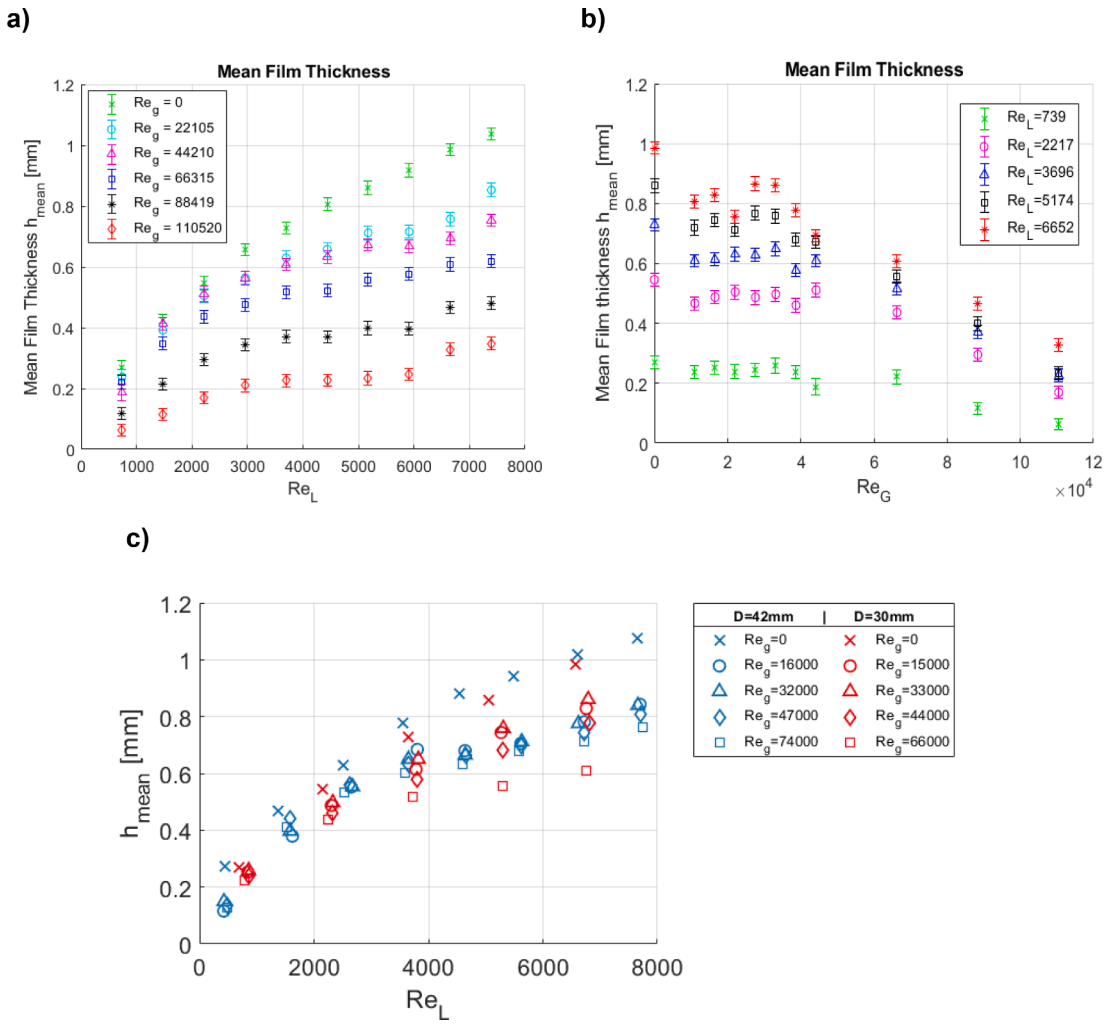

Fig. 9. Mean Film Thickness (h_m) evolution versus a) liquid Reynolds number for different gas Reynolds numbers; b) gas Reynolds number for several liquid Reynolds numbers; c) liquid Reynolds number comparing both pipe diameters.

these two variables of the disturbance wave. In particular, a peak calculation algorithm based on three restrictions was applied during the processing. The principal objective of the procedure is to discard from the disturbance wave counting not only the ripples waves but also multiple close crest peaks.

The first criterion is carried out by establishing a threshold value from which the wave is taken as a disturbance wave (De Jong and Gabriel, 2003; Rodriguez and Shedd, 2004; Cuadros et al., 2019; Rivera et al., 2021), i.e., peaks that are below the threshold value are removed. This threshold value depends on the flow characteristics. For instance, the mean film thickness has been chosen as the cutting value for this research, as displayed in Fig. 10.

The following consideration is a proximity criterion, implemented to avoid multiple nearby peaks, a situation that mainly occurs in the wave crests vicinity (Cuadros et al., 2019; Rivera et al., 2021). The value applied to consider this closeness criterion depends on the temporal resolution of the measurement system and the characteristics of the waves, then, a minimum distance between successive DW peaks is defined, $d_{min,DW}$, so where the maximum distance between two consecutive DWs is less than this value, only the larger one is taken into account, as also shown in Fig. 10.

Finally, a prominence criterion has been designed to discard low amplitude peaks, those that are located between DWs (Cuadros et al., 2019; Rivera et al., 2021). Suppose the relative height of a minor peak is less than this prominence cut-off value. In that case, the minor peak is considered a ripple wave overlapped with some part of a DW, and consequently, this second peak is removed, as displayed in Fig. 10. A gas Reynolds number dependent prominence value has been established. A value ranging from 0.2 for free fall to 0.05 for the maximum gas Reynolds number understudy has been established. For large Reynolds numbers, the relative height of the disturbance waves decreases, so the prominence value has been reduced accordingly.

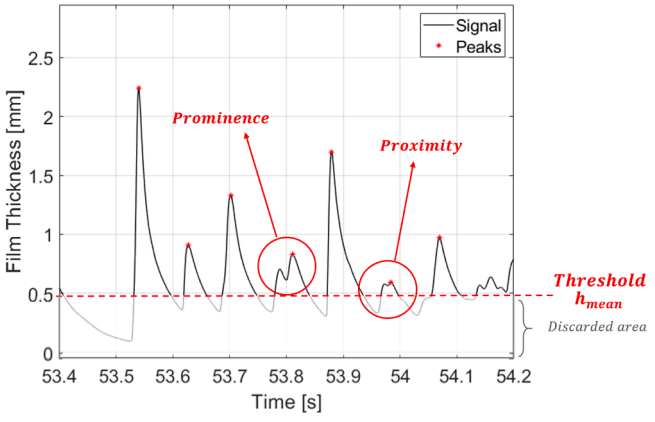

Fig. 10. Representation of the multi-criteria used to a one-second data.

4.3.1. Disturbance wave heights

DWs have been identified after applying these three criteria. Fig. 11 displays examples of the estimations of the DWs' heights as a function of the gas and liquid Reynolds numbers for both pipe diameters.

In the case of the disturbance wave amplitudes, as intuitively could be thought out, an inverse trend of the wave amplitudes with the gas flow rates should exist, as displayed in Fig. 11a. While, there should exist a direct trend for the liquid flow rate, as displayed in Fig. 11b. This wave amplitude dependence is much more pronounced with gas velocities, as shown in Fig. 11, being less dependent on the total inlet water flow. Although, when analysing the experimental data, maximum values of the disturbance wave heights have been measured at approximately $2{\cdot}10^4$-$4{\cdot}10^4$ gas Reynolds numbers depending on the liquid Reynolds number. Fig. 11c shows the DW height obtained for each pipe diameter. It can be seen that the measurements follow a similar trend, although, for high Reynolds numbers of the gas, substantial differences can be seen. This comparison would slightly change if only the air surface velocity was considered. However, this study has attempted to maintain the highest degree of generality for potential comparisons with studies under different conditions.

As commented above, the changes in the wave amplitude behaviour observed for the liquid film thickness is mainly caused by the gravity effect and the shear stress between the liquid and the gas phases. There is an increase in wave height as the gas velocity increases. This increase stops when the Reynolds values of the gas reach around $Re_{g\_maxhDW} = 2{\cdot}10^4$-$4{\cdot}10^4$. From this point on, the wave height decreases as the interaction between the gas and the liquid increases.

Most classical studies already pointed to a transition between the downward annular flow sub-regimes. The "regular wave" regime (also observed in upward annular flow) appears for gas Reynolds numbers higher than the Re_{g_maxhDW} value described in this paper. The authors Webb and Hewitt (1975) explained that only one type of well-defined disturbance wave is observed in this zone, and the gas–liquid interaction predominates. For lower Re_g values, different sub-regimes can occur, such as the "dual-wave", where two types of DW are distinguished. The first type is observed in free-fall and a second type becomes more and more predominant as the velocity increases until the critical zone. More recent studies, such as Cherdansev et al. (2019), point to bubble trapping in the liquid film. This happens due to the agitation produced by the gas, which becomes particularly significant in the critical zone of regime change.

Consequently, in order to capture the variation in the position of this maximum, multiple fits were made for the disturbance waves as a function of the gas Reynolds numbers for each liquid Reynolds number. Then, these maximums of all liquid Reynolds numbers have been correlated using a linear fit (Fig. 12):

$$Re_{G\_maxhDW} = 27252 - Re_L \tag{11}$$

4.3.2. Disturbance wave frequencies

The last issue to be obtained from the experimental measurements is

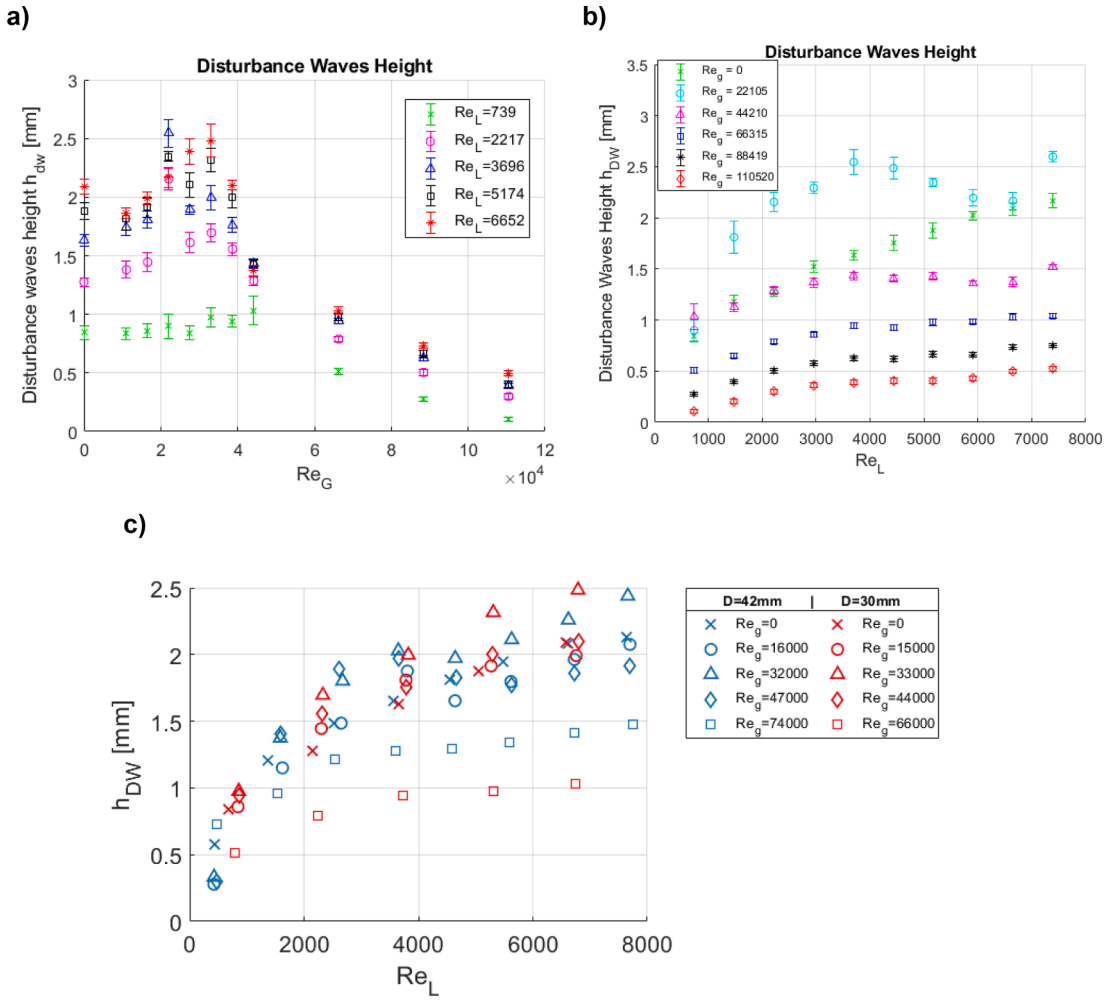

Fig. 11. Disturbance Wave Height (h_{DW}) evolution as a function of: a) gas Reynolds number for different liquid Reynolds numbers; b) liquid Reynolds number for different gas Reynolds numbers; c) liquid Reynolds number, comparing both pipe diameters.

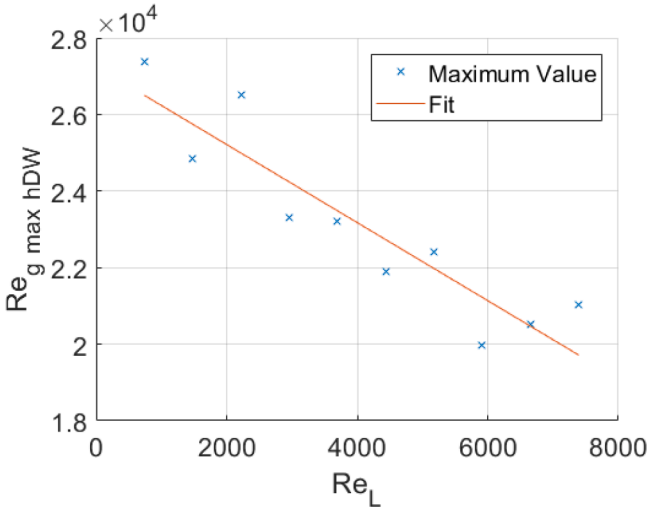

Fig. 12. Fitting line of gas Reynolds number at which the maximum disturbance wave amplitudes takes place as function of the liquid Reynolds number.

the DWs frequency. The mean frequency value was estimated by calculating the number of peaks per second, counting the number of DW peaks and dividing by the measurement time interval for each experimental condition.

Fig. 13 displays the trend dependencies of the DW frequency for the different gas and liquid Reynolds numbers studied. The frequency range covers from 2 to 18 Hz approximately. The lower frequency values are for the lower liquid flow rates and moderately low gas Reynolds numbers.

The frequency evolution with the gas Reynolds number follows a similar behaviour to DW height. Initially, as the gas Reynolds number increases, a downward trend in frequency is observed. However, at about the Re_{g_maxhDW} described above, there is a sharp increase in frequency. This increase tends to stabilise at a gas Reynolds number of $6{\cdot}10^4$ and above, independently of the liquid flow rate.

Although the explanation is not as simple, the velocity difference between disturbance waves and gas plays an important role. The downward annular flow does not require moving air as gravity generates the movement naturally. The transition from a flow governed by gravity to one influenced by air flow is related to this behaviour of the characteristic variables. Nevertheless, with these reasons alone, it is difficult to explain why a reduction in wave frequency and an increase in height are observed. A more detailed future investigation of this question is probably desirable in order to be able to make a statement on the matter.

When comparing the frequency obtained in the 30 mm and 42 mm diameter test sections (Fig. 13c), it can be observed that both follow the same pattern. A higher frequency is observed in free fall than during the transition zone. Yet again, the frequency increases in both cases for higher gas Reynolds numbers.

Additionally, it must be commented the huge error bar existent in a

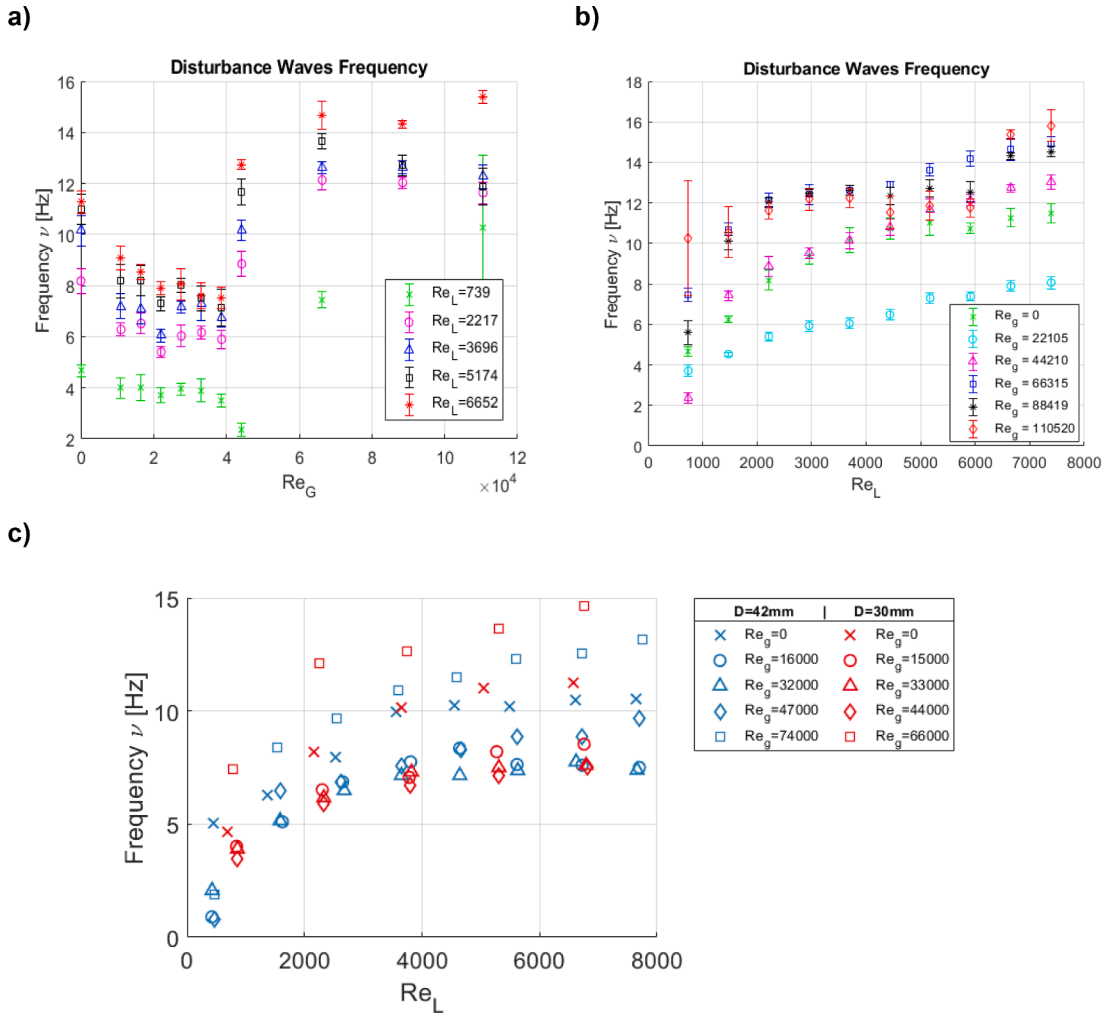

Fig. 13. Disturbance Wave Frequency (υ_{DW}) evolution as a function of: a) gas Reynolds number for different liquid Reynolds numbers; b) liquid Reynolds number for different gas Reynolds numbers; c) liquid Reynolds number, comparing both pipe diameters.

point of Fig. 13. This mistake is caused by the fact that this point is the lowest liquid flow and highest gas flow. Consequently, as the liquid film is so thin and the gas flow is so high, then high variability of the wave frequency between the six experimental series of ten seconds each one has been obtained. However, the averaged values of the wave frequencies are apparently around the expected value.

5. Discussion of results and correlations

This section focuses on analysing and estimating trends between inlet conditions and other fluid variables with the major film properties, leading to the definition of correlations between them. Several correlations have been developed to determine the water film thicknesses and the interfacial characteristics. The main variables considered in this paper are the mean liquid film thickness (h_{mean}), the DW height (h_{DW}) and the DW frequency (ν_{DW}). When carrying out these types of analyses, dimensionless numbers are strongly recommended. Consequently, dimensionless numbers have been used to characterise all the considered flow magnitudes. All these interfacial characteristics, film thicknesses and wave characteristics result from a dynamic equilibrium between disturbance forces that perturb the flat surface (inertial forces) and the forces opposing the alteration of the surface (related to surface tension and viscosity). Then, as it is inferred in the current study and as it is also widely recognised, the behaviour of interfacial waves inside tubes is very chaotic. Then, in order to characterise film thicknesses and wave behaviours, several dimensionless numbers have been analysed. In particular, their dependence on Reynolds, Froude and Weber numbers have been tested. But, in order to reduce as much as possible the complexity of the correlation, the expressions with the lowest number of dimensionless numbers and the highest determination coefficient (R^2) has been given as a final result, achieving a very good correlation using only gas and liquid Reynolds numbers. In addition, the Strouhal number has been used in the estimation of the wave frequencies.

5.1. Mean liquid film thickness discussion

To characterise the liquid film in downward annular flow, the first variable on which the analyses are usually focused is the average film thickness (h_{mean}). This variable corresponds to the average distance between the wall and the air–water interface (Fig. 7). The data analysis has been carried out to study this variable, and a new correlation has been developed. The current experimental data and their correlation curve are displayed against theoretical expressions. In addition, other experimental data found in the literature have been displayed, as well as other experimental expressions.

5.1.1. Correlation of the mean liquid film thickness

This subsection shows the result of relating the h_{mean} to the experimental conditions through a correlation. For this purpose, the experimental measurements were approximated by a function using the input properties. In order to maintain generality and to make the data more accessible, only dimensionless numbers have been used to calculate the mean film thickness.

First, we correlated the free-falling data for both pipe diameters and their respective experimental conditions. The new correlation obtained is given by:

$$\frac{h_{mean}}{L_m} = 0.19 \cdot Re_L^{0.54} \tag{12}$$

where L_m is the viscous-gravity length, which is defined as.

$$L_m = \left(\frac{\upsilon^2}{g sin\beta}\right)^{1/3} \tag{13}$$

in our case, the flow is vertical, $\beta = 90°$ so $\sin\beta = 1$.

Eq. (12) shows that the film thickness can be calculated using the properties of the liquid and its conditions at the inlet. Fig. 14 shows the comparison between the data obtained by the new correlation represented as $Fith_{mean}$ and the experimental measurements. As can be seen, the new correlation fits the experimental data very accurately, and all measured points are within the ± 10% error band. The R^2 coefficient corresponding to the Pearson product-moment coefficient is 0.985, and the RMS error is 0.0135.

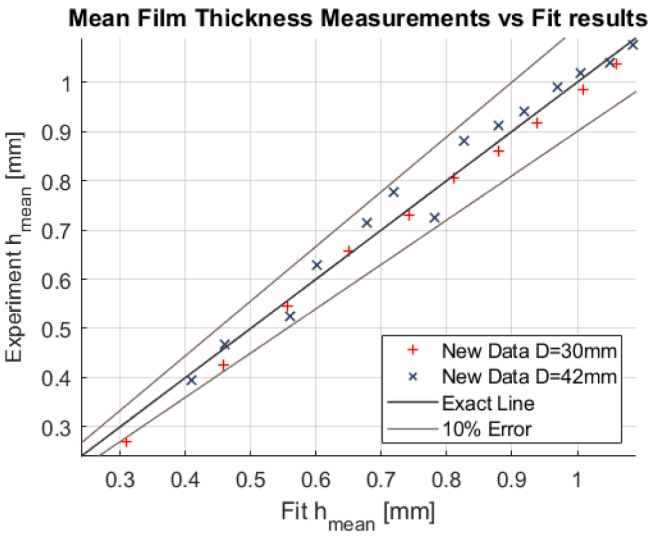

Fig. 14. Experimental mean film thickness vs data obtained with the new correlation for free falling conditions.

If the cocurrent downward flow data are added to the free falling ones, then only a new term in Eq. (12) is needed to capture the influence of these new conditions. As a result, the following correlation is obtained:

$$\frac{h_{mean}}{L_m} = 0.19 \cdot Re_L^{0.54} \cdot \left(1 - 1.29 \cdot 10^{-5} \cdot Re_G^{0.93}\right) \tag{14}$$

Fig. 15 compares the data obtained by this new correlation and the experimental measurements. The new correlation fits fairly accurately the experimental data, with all points found within the ± 30% error bands. As before, R^2 has been calculated, obtaining a value of 0.939, and the RMS error is 0.055.

As discussed in the previous section, it is important not only to study the film thickness under fully developed flow conditions but also under

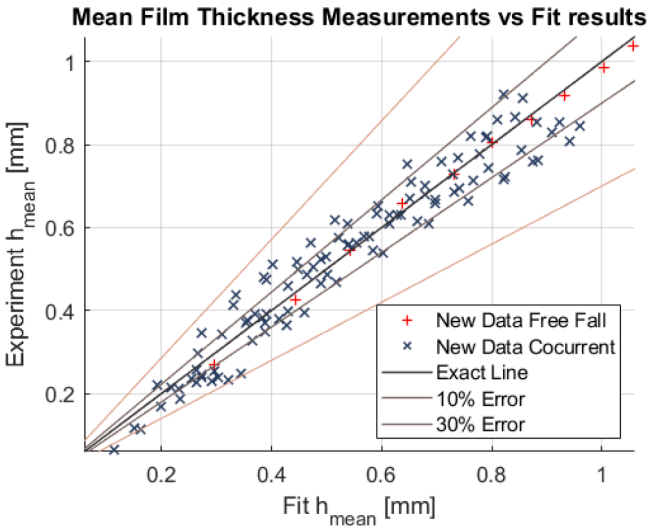

Fig. 15. Experimental mean film thickness vs. data obtained with the new correlation for cocurrent downward conditions.

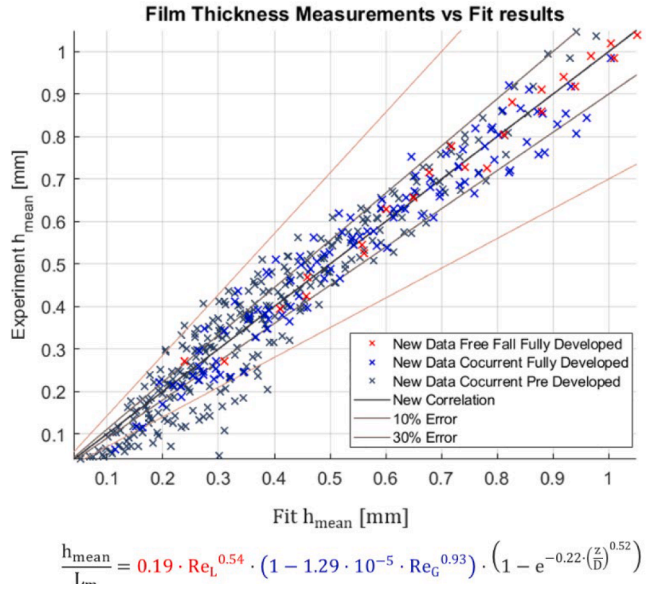

Fig. 16. Experimental mean film thickness vs. data obtained with the new correlation for cocurrent conditions considering the developed and developing regions.

flow developing conditions. Consequently, the consideration of the development region is of interest, so in order to study the influence of this region, the corresponding data have been added to the previous ones. The result is an additional term in Eq. (14) that captures the influence of the developing flow conditions. Finally, the following correlation has been obtained:

$$\frac{h_{mean}}{L_m} = 0.19 \cdot Re_L^{0.54} \cdot \left(1 - 1.29 \cdot 10^{-5} \cdot Re_G^{0.93}\right) \cdot \left(1 - e^{-0.22 \cdot \left(\frac{z}{D}\right)^{0.52}}\right) \tag{15}$$

Then, following the same procedure as for the free-fall and cocurrent correlations, the data obtained by applying the correlation and the experimental data have been compared (Fig. 16). As for the previous cases, the new correlation has a quite good data fitting since most data are inside the 30% error band, with a Pearson product-moment correlation coefficient of $R^2 = 0.895$ and an RMS error of 0.071.

5.1.2. *Performance of the new correlations against other correlations and experimental data*

The data and correlations obtained in this research have been compared in detail with studies by other authors. On the one hand, the correlations proposed in this paper have been used to check whether they are able to predict the experimental results of other research groups. On the other hand, the experimental correlations proposed by other authors have been studied to verify their predictive potential for our measurements. Table 3 summarises the empirical expressions to calculate the average film thickness and some details related to the conditions to use it.

Theoretical models to estimate the film thickness under free falling conditions have been developed within over a hundred years. Specifically, Nusselt's model provided the first and up to now more widely used estimation of the liquid thickness under laminar conditions (Nusselt, 1916a,b). Nusselt's theory supposes not only laminar but also smooth and two-dimensional flow on an infinite flat plate, the expression is:

$$\frac{h_{mean}}{L_m} = \left(\frac{3}{4} Re_L\right)^{1/3} \tag{16}$$

Padmanaban, in his PhD (2006), provides a good summary of liquid film expressions. For instance, Bergelin's theoretical expression, valid for the turbulent regime.

$$(3.0 + 2.5 \cdot ln\bar{\delta}^{+})\bar{\delta}^{+} = \frac{Re_L}{4} + 64 \tag{17}$$

in which the non-dimensional film thicknesses is defined as,

$$\bar{\delta}^{+} = \frac{\rho \cdot u^{*} \cdot h_{mean}}{\mu_l} \tag{18}$$

being the frictional velocity defined from a force balance between wall friction and gravity forces:

$$u^{*} = \sqrt{\frac{\tau_w}{\rho}} = \sqrt{g \cdot h_{mean}} \tag{19}$$

The transition laminar-turbulent was also determined by Dukler and Bergelin (Padmanaban, 2006), a liquid Reynolds number of 1080 was proposed. In contrast, other researchers' studies propose higher values, such as Fulford, which gives a value of 2360 to the laminar-turbulent transition to begin. A criterion to estimate the transition from laminar to turbulent flow is also available (Mudawwar and El-Masri, 1986):

$$Re_{crit} = 97 Ka^{0.3} \tag{20}$$

In which the Kapitza number is defined in the usual form,

$$Ka = \frac{\sigma}{\rho g^{1/3} \nu^{4/3}} \tag{21}$$

Kapitza's theoretical expression can be used for smooth wavy laminar flows (Aliyu, 2015), which accounts for the effects of regular periodic waves and surface tension. The proposed equation is a modification of Nusselt's theory to account for the influence of shear stresses and interfacial waves:

$$h_{mean} = \left(\frac{2.4}{4} \frac{\upsilon^2}{g} Re_L\right)^{1/3} \tag{22}$$

For the turbulent region, many experimental correlations are available in the literature, in particular, a considerable number of semi-empirical correlations based on the form of Nusselt's theory have been proposed over the last decades, almost all of them having the following form:

$$h_{mean} = A \left(\frac{\upsilon^2}{g}\right)^{1/3} Re_L^B \tag{23}$$

In which A and B are regression constants. For instance, Mudawwar and El-Masri (1986) defined a semi-empirical correlation for the mean liquid film thickness estimation:

$$h_{mean} = 0.065 \left(\frac{\upsilon^2}{g}\right)^{1/3} Re_L^{0.58} \tag{24}$$

If a gas stream is introduced in cocurrent with the free falling water flow, the number of available correlations are much more reduced. Henstock and Hanratty (1976) correlated most of the previous studies carried out for horizontal and vertical flows. The proposed correlation for vertical flows, both downward and upward, is:

$$\frac{h_{mean}}{D} = \frac{6.59F}{(1 + 1400F)^{1/2}} \tag{25}$$

where the parameter F is given by.

$$F = \frac{\upsilon_l}{\upsilon_g} \left(\frac{\rho_l}{\rho_g}\right)^{1/2} \frac{\gamma(Re_L)}{Re_g^{0.9}} \tag{26}$$

and

$$\gamma(Re_L) = \left[\left(0.707 Re_L^{1/2}\right)^{5/2} + \left(0.0379 Re_L^{9/10}\right)^{5/2}\right]^{2/5} \tag{27}$$

Table 3
Summary of Mean Film Thickness expressions.

Reference	Expression	Conditions
Free Falling Flow		
Nusselt (1916a,b) (Nusselt 2016a,b)	$\frac{h_{mean}}{L_m} = \left(\frac{3}{4}\,Re_L\right)^{1/3}$	Theoretical, laminar regime, smooth flow and infinite flat plate
Dukler and Bergelin (1952) (Takahama and Kato, 1980)	$(3.0 + 2.5\cdot\ln\bar{\delta}^{+})\bar{\delta}^{+} = \frac{Re_L}{4} + 64;$ $\bar{\delta}^{+} = \frac{\rho\cdot u^{*}\cdot h_{mean}}{\mu_l};\ u^{*} = \sqrt{\frac{\tau_w}{\rho}} = \sqrt{g\cdot h_{mean}}$	Theoretical, turbulent regime (Re_L greater than 1080), flat plate, pipe
Brotz (1954)* (Padmanaban, 2006)	$\frac{h_{mean}}{L_m} = 0.641 Re_L^{2/3}$	Re_L = 2360–17200, pipe inside,$\upsilon = 10^{-6} - 8.48\cdot10^{-6} m^2/s$
Kapitza (1965) (Aliyu, 2015)	$\frac{h_{mean}}{L_m} = \left(\frac{2.4}{4} Re_L\right)^{1/3}$	Theoretical, regular periodic waves and surface tension, smooth wavy laminar
Brauer (1956) * (Takahama and Kato, 1980)	$\frac{h_{mean}}{L_m} = 0.208\ Re_L^{8/15}$	Re_L = 1600–7200, pipe outside (o.d. 43 mm), $\upsilon = 0.9\cdot10^{-6} - 12.7\cdot10^{-5} m^2/s$
Feind (1960)* (Padmanaban, 2006)	$\frac{h_{mean}}{L_m} = 0.266\ Re_L^{1/2}$	Turbulent regime, pipe inside (20, 50 mm i.d.), $\upsilon = 10^{-6} - 1.97\cdot10^{-5} m^2/s$
Hanratty and Hershman (1961)* (Padmanaban, 2006)	$\frac{h_{mean}}{L_m} = 0.141\ Re_L^{7/12}$	Re_L = 600–14000, pipe inside (20 mm i.d.)
Takahama * (Takahama and Kato, 1980)	$\frac{h_{mean}}{L_m} = 0.228\, Re_L^{0.526}$	Re_L = 600–8000, pipe inside
Mudawwar * (Mudawwar and El-Masri, 1986)	$\frac{h_{mean}}{L_m} = 0.145\, Re_L^{0.58}$	Semi-empirical model, turbulent flow
Brauner (1987) * (Brauner, 1987)	$\frac{h_{mean}}{L_m} = \left(\frac{3}{8} Re_L\right)^{1/3}$ (Laminar Region) $\frac{h_{mean}}{L_m} = 0.104\, Re_L^{7/12}$ (Turbulent Region)	Theoretical, harmonic and infinitesimal waves
Karapantsios et al. (1989) *(Padmanaban, 2006)	$\frac{h_{mean}}{L_m} = 0.214\, Re_L^{0.538}$	Re_L = 504–13100, pipe inside
Pagmanaban * (Padmanaban, 2006)	$\frac{h_{mean}}{L_m} = 0.1855\, Re_L^{0.558}$	Re_L = 4000–20000, pipe inside
Aliyu (Aliyu, 2015)*	$\frac{h_{mean}}{L_m} = 1.4459\, Re_L^{0.3051}$	Re_L = 4000–20200, pipe inside, large diameter (101.6 i.d.)
New Correlation, Eq. (12)	$\frac{h_{mean}}{L_m} = 0.19\cdot Re_L^{0.54}$	Re_L = 560–11300, pipe inside (30, 42 mm i.d.)
Cocurrent Downward Flow		
Henstock and Hanratty, (Henstock and Hanratty, 1976)	$\frac{h_{mean}}{D} = \frac{6.59\,F}{(1+1400F)^{1/2}} F = \frac{\upsilon_l}{\upsilon_g}\left(\frac{\rho_l}{\rho_g}\right)^{1/2} \frac{\gamma(Re_L)}{Re_G^{0.9}} \gamma(Re_L) = \left[\left(0.707 Re_L^{1/2}\right)^{5/2} + \left(0.0379 Re_L^{9/10}\right)^{5/2}\right]^{2/5}$	Vertical upward and downward, Re_L = 20–15100, Re_G = 5000–255000, pipe inside (25.4, 50.8, 63.5 mm i.d.),
Kulov et al. (1979)*, (Kulov et al., 1979)	$\frac{h_{mean}}{L_m} = 0.266\, Re_L^{0.6} Re_G^{-0.1}; 8000 \le Re_G \le Re_G^{*} \frac{h_{mean}}{L_m} = 62.6\, Re_L^{0.52} Re_G^{-0.61}; Re_G^{*} \le Re_G \le 85000 Re_G^{*} = 5.32 \bullet 10^{4} Re_L^{-0.19}$	$Re_L \le$ 13000, Re_G = 8000–85000,pipe inside (25 mm i.d.),$\upsilon = 10^{-6} - 10^{-5} m^2/s$
Czernek and Witczak (2020)*, (Czernek and Witczak, 2020)	$h_{mean} = h_0 \frac{1}{1 + 5.68\cdot10^{-3} Re_L^{0.132} Re_G^{0.47}} h_0 = 0.852\, L_m\, Re_L^{0.516}\ ;\ Re_L < 2\ h_0 = 0.9335\, L_m\, Re_L^{0.334}\ ;\ Re_L > 2$	J_L = 0 – 0.254 m/s, J_G = 0–29.9 m/s, pipe inside (12.5, 16, 22 and 54 mm i.d.), $\mu = 0.055 - 1.517 Pas$,
New Correlation, Eq. (13)	$\frac{h_{mean}}{L_m} = 0.19\cdot Re_L^{0.54}\cdot\left(1 - 1.29\cdot10^{-5}\cdot Re_G^{0.93}\right)$	Re_L = 560–11300, Re_G = 0–1.1·10^5, pipe inside (30, 42 mm i.d.)
Cocurrent Downward Flow developing and developed regions		
New Correlation, Eq. (14)	$\frac{h_{mean}}{L_m} = 0.19\cdot Re_L^{0.54}\cdot\left(1 - 1.29\cdot10^{-5}\cdot Re_G^{0.93}\right)\cdot\left(1 - e^{-0.22\cdot\left(\frac{z}{D}\right)^{0.52}}\right)$	Re_L = 560–11300, Re_G = 0–1.1·10^5, pipe inside (30, 42 mm i.d.)

*correlations developed for vertical flows which do not use the definition of the viscous-gravity length, $L_m = \left(\frac{\upsilon^2}{g sin\beta}\right)^{1/3}$, but directly $\left(\frac{\upsilon^2}{g}\right)^{1/3}$.

The correlated data, only those of vertical downward flows, covered the following experimental conditions: liquid Reynolds numbers between 20 and $1.51{\cdot}10^4$; gas Reynolds number between 5000 and $2.55{\cdot}10^5$; and inner pipe diameters of 25.4, 50.8 and 63.5 mm.

Kulov et al. (1979) carried out investigations with water-glycerol mixtures ($\upsilon = 10^{-6} - 10^{-5} m^2/s$), liquid Reynolds numbers up to $5{\cdot}10^4$ were studied, and gas Reynolds numbers up to $8.5{\cdot}10^4$. The authors proposed the following correlations:

$$h_{mean} = 0.266\left(\frac{\upsilon^2}{g}\right)^{1/3} Re_L^{0.6} Re_G^{-0.1}; 8000 \le Re_G \le Re_G^* \tag{28}$$

$$h_{mean} = 62.6\left(\frac{\upsilon^2}{g}\right)^{1/3} Re_L^{0.52} Re_G^{-0.61}; Re_G^* \le Re_G \le 85000 \tag{29}$$

being Re_G^* a threshold Reynolds number which divides the two flow regions and is given by $Re_G^* = 5.32{\cdot}10^4 \mathrm{Re}_L^{-0.19}$.

Czernek and Witczak (2020) have proposed another correlation, but applicable for very viscous liquids in the range ($\mu = 0.055 - 1.517 Pa{\cdot}s$), the correlation is as follows:

$$h_{mean} = h_0 \frac{1}{1 + 5.68{\cdot}10^{-3} Re_L^{0.132} Re_G^{0.47}} \tag{30}$$

where the reference film height, h_0, is given by:

$$h_0 = 0.852\left(\frac{\upsilon^2}{g}\right)^{1/3} Re_L^{0.516}; Re_L < 2 \tag{31}$$

$$h_0 = 0.9335\left(\frac{\upsilon^2}{g}\right)^{\frac{1}{3}} Re_L^{0.334}; Re_L > 2 \tag{32}$$

The consideration of the development region is of interest, but this region is strongly influenced by the inlet conditions of both gas and liquid phases. In our case, the liquid has been introduced as a thin layer on the pipe wall and the gas phase in the central section of the pipe. This configuration could simulate the conditions of different technological systems, like in heat exchangers. However, no data or expression has been found addressing this issue. Consequently, all three configurations, free falling, forced falling and developing region, have been analysed in this section.

Fig. 17 focuses on free falling flows, widely investigated over the last century. The figure shows that all the experimental data closely follow Nusselt's expression for low liquid Reynolds numbers (Nusselt, 1916a, b). However, as the flow gradually becomes turbulent, the expression's estimations underestimate the experimental data. Many expressions to estimate the liquid film thickness in this region are available in the literature (most of them summarised in Table 3). Besides, a considerable number of experimental data are available too (Webb and Hewitt, 1975; Takahama and Kato, 1980; Karapantsios et al., 1989, Karapantsios and Karabelas, 1995; Karimi and Kawwaji, 1998; Zadrazil et al., 2014; Cherdansev et al., 2019; Charogiannis et al., 2019). Not only are all data close to each other (Fig. 17), but all the proposed correlations predict similar values. Consequently, falling films are considered to be fairly well characterised. In fact, only Karimi's data, whose experiments were performed using kerosene instead of water, differ appreciably. Those data suggest the existence of thicker liquid layers for kerosene than for water at the same liquid Reynolds numbers.

Fig. 18 displays the performance of the new developed expression against the experimental data of several researchers data for downward cocurrent flow conditions. As seen in the figure, there is a much larger scatter between the experimental data and the correlation predictions. However, in general, the values of the different authors are captured adequately. The Zadrazil et al. (2014) and the Cherdansev et al. (2019) data are quite well captured by the current proposed correlation. The only significant discrepancies are those found in the Vasques et al. (2018), which are systematically underestimated by the new proposed correlation. This difference is probably due to the significant difference in diameters between installations, which impacts the gas Reynolds number term.

Fig. 19 shows the predictions for the different expressions proposed by several researchers with those of the currently developed expression for downward cocurrent flows. As shown in the figure, there are significant differences when comparing the different expressions. In particular, the highest discrepancies are with Czernek's correlation. This expression systematically underestimates the thickness of the liquid layer. This result may be justified since this correlation was developed for high surface tension liquids, particularly several types of oils. The currently developed correlation, which gives the best results when compared with the present experimental data, predicts slightly higher values than Henstock's expression for almost all values of the liquid and gas Reynolds numbers covered. Only for small values of both Reynolds numbers does the Henstock expression exceed the values of the new correlation predictions. In contrast, Kulov's correlation provides lower values than Henstock's and the current correlation for almost all gas and liquid Reynolds numbers covered.

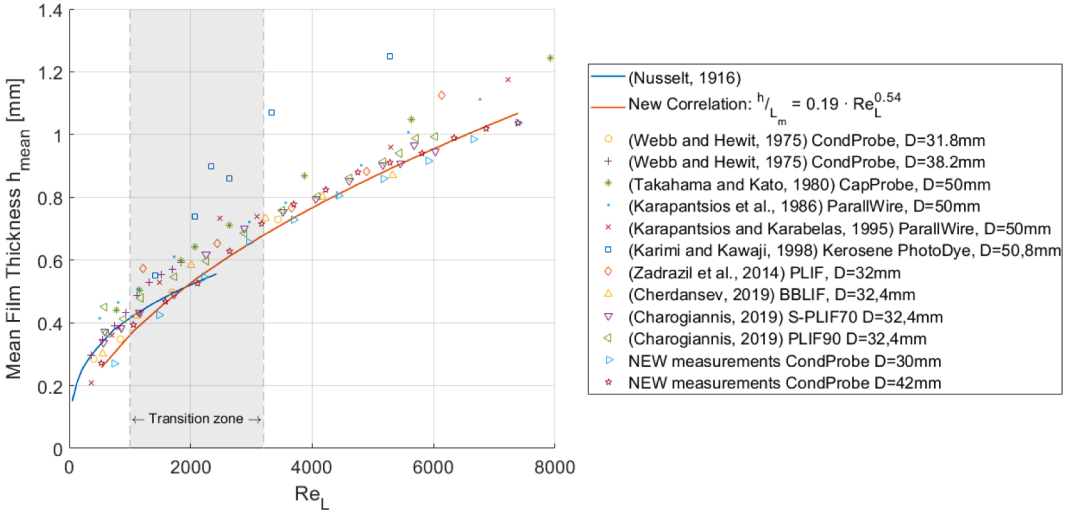

Fig. 17. Comparison of the mean film thickness obtained by different authors as a function of the Reynolds number of the liquid under Free Falling conditions. The theoretical expression of Nusselt and the empirical correlation proposed in this paper have also been included.

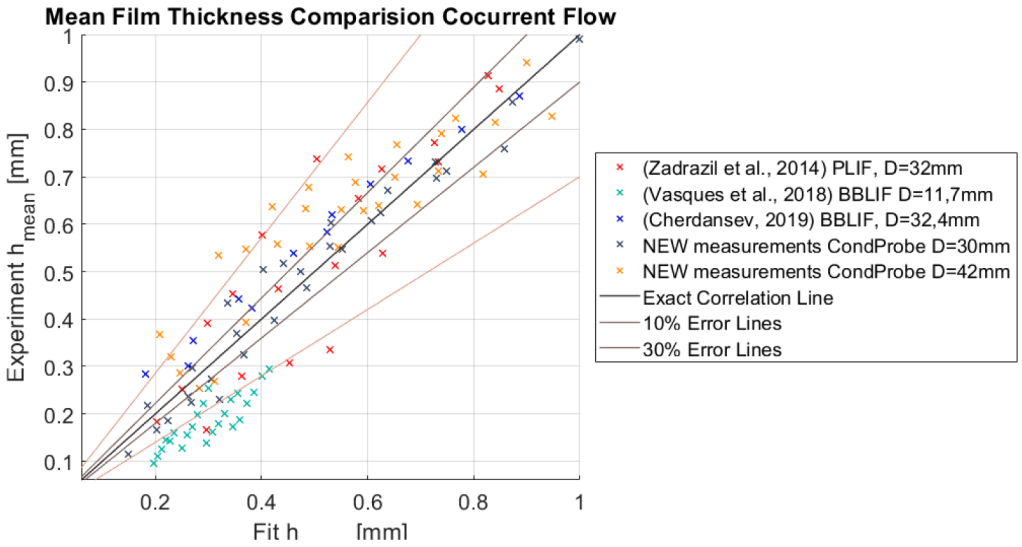

Fig. 18. Experimental data of the Mean Film Thickness versus the predictions of the new correlation under Cocurrent Downward Flow conditions.

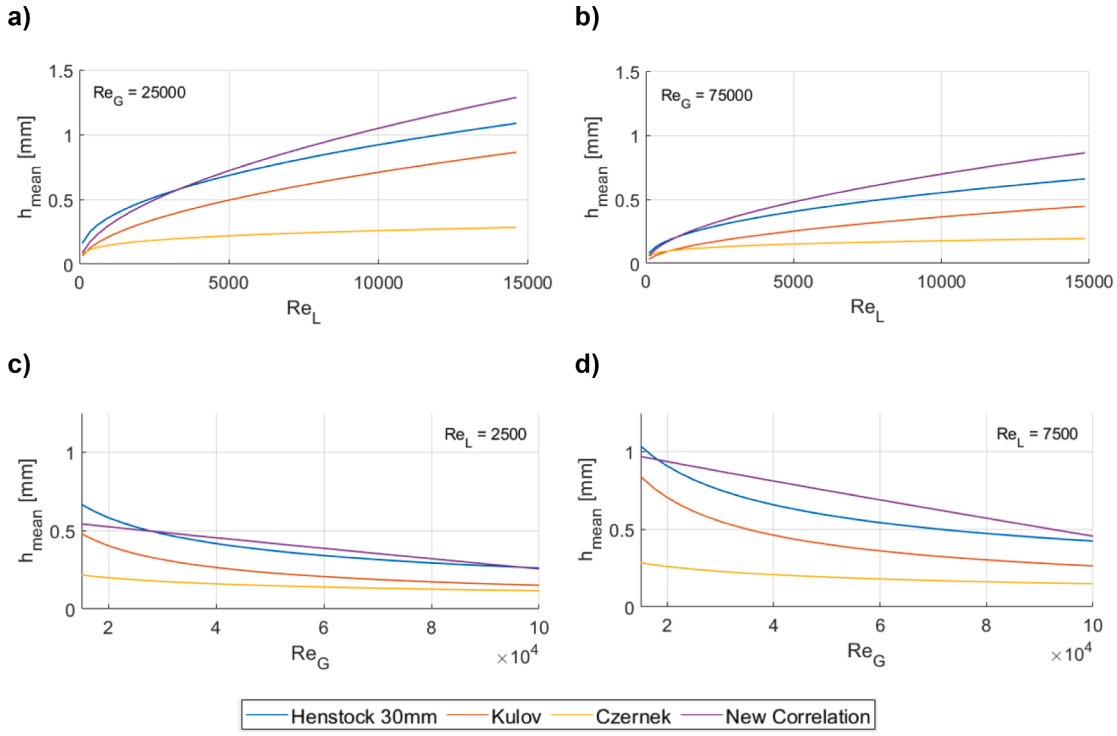

Fig. 19. Comparison of the Mean Film Thickness obtained according to the empirical correlations proposed by different authors as function of: a-b) Liquid Reynolds number at constant Gas Reynolds number; c-d) Gas Reynolds number at constant Liquid Reynolds number.

5.2. Disturbance waves discussion

This section focuses on analysing some of the most important characteristics of DWs. In particular, empirical expressions have been proposed to calculate the average height of the waves as well as the frequency at which they appear. Similar to the procedure in the previous sections, these expressions have been calculated as a function of dimensionless numbers not to lose generality. We have checked the effects of using different dimensional numbers in this adjustment process. However, since the adjustments were very good only using the gas and liquid Reynolds numbers, we have chosen not to increase the complexity of the correlations and present them according to these two dimensionless numbers only.

5.2.1. Disturbance wave heights

The height of the disturbance waves is defined as the average distance between the wave peaks and the pipe wall. Only the peaks of the DWs have been taken into account, discarding the peaks of the RWs.

5.2.1.1. Correlation of the disturbance wave height measurements. The empirical correlation proposed that best fits the experimental measurements is:

$$\frac{h_{DW}}{L_m} = 2.6 \cdot Re_L^{0.35} \cdot \left(1 - 5.8 \cdot 10^{-5} \cdot abs(Re_G - Re_{G\_maxhDW})^{0.845}\right) \quad (33)$$

in which the DWs height has been calculated as a function of the liquid

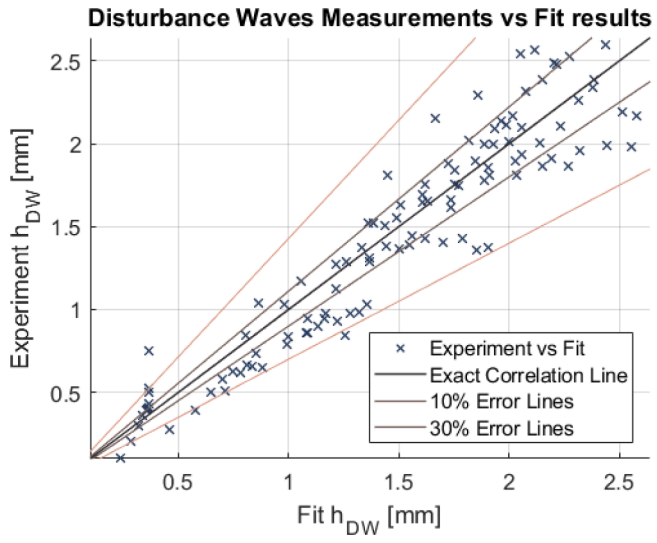

Fig. 20. Experimental DW heights vs. data obtained with the new correlation.

and gas Reynolds numbers defined in Eq. (5) and Eq.(4) respectively, and the Re_{G_maxhDW}. This term corresponds to the gas Reynolds number at which the maximum wave height is reached as a function of the liquid Reynolds number, Eq. (11).

The fitting correlation, Eq. (33), and the experimental data are displayed in Fig. 20. As can be seen, the new correlation predicts with fairly good accuracy the experimental measurements, finding a large number of points in the ± 10% error bands and most of them within the ± 30% error bands. The value of the determination coefficient R^2 is 0.881 and the RMS error is 0.2276.

The tendency observed for the height of the DWs is quite similar to the trend previously explained for the average film thickness. The height of the waves grows as the liquid Reynolds number increases. However, when we observe the behaviour of the height as the Reynolds number of the gas varies, the value increases up to a certain number and then decreases rapidly. This behaviour has already been explained in section 4.2.1 where its reasoning is detailed.

5.2.1.2. New correlation performance against other correlations and experimental data. Very limited expressions to estimate the wave height are available in the literature. Most of them apply to free-falling films or low liquid Reynolds numbers. Nosoko et al. (1996) propose the following correlation of the wave peak height for free-falling films in a vertical flat plate:

$$h_{DW} = 0.49 \cdot \left(\frac{\upsilon^2}{g}\right)^{1/3} K_F{}^{0.044} N_\lambda{}^{0.39} Re_L^{0.46} \tag{34}$$

where K_F is the dimensionless group of physical properties and N_λ is the dimensionless wave separation, which are defined as:

$$K_F = \frac{\rho^3 \nu^4 g}{\sigma^3} \tag{35}$$

$$N_\lambda = \lambda \left(\frac{g}{\nu^2}\right)^{1/3} \tag{36}$$

being λ the separation between neighbouring composite waves. The covered range of liquid Reynolds numbers was from 14 to 90.

Other authors propose analytical expressions, like Chang, Nguyen or Panga. Chang used the Nakaya model and proposed an analytical expression (Nguyen and Balakotaiah, 2000) based on a non-linear treatment of longwave approximation. Nguyen and Balakotaiah (2000) proposed a model which is based on a boundary-layer analysis and describes the characteristics of free-falling films, especially for low liquid Reynolds numbers (Re_L = 2–20) and low Kapitza numbers (Ka = 6–22). Panga et al. (2005) proposed a new scaling method to reduce the Navier-Stokes equations to a single evolution equation for the scaled film thickness, h(x,t). Near the double zero singularity, there is the homoclinic bifurcation and using Melnikov's analysis, the authors obtained an expression for the maximum wave amplitude of the solitary waves. All these models have a restricted applicability region, far from the current data, and also have the same form:

$$h_{max} - 1 = AWe \tag{37}$$

being A equal to 7.56, 1.925 and 2.52 respectively, and the Weber number is defined in terms of the mean film thickness of Nusselt's expression:

$$We = \frac{\rho u^2 h_{mean,Nusselt}}{\sigma} \tag{38}$$

Meza and Balakotaiah (2008) explains that for viscous fluids ($2 < Ka < 200$), there is an increasing tendency of the wave amplitudes with the Weber number, with a saturation value at around $h_{max}/h_{mean,Nusselt} = 3$, having a weak dependency on the Kapitza number. While for less viscous fluids ($200 < Ka < 3890$), the waves are found to be much more dynamic and pronounced, having bigger amplitudes, which saturate at around values of $h_{max}/h_{mean,Nusselt} = 10$.

Holowach et al. (2002) propose a theoretical expression for estimating the wave amplitude. This expression is dependent on fluid properties and the interfacial shear stresses. The methodology was initially proposed by Ishii and Grolmes (1975) and assumes that a shear flow model can express the wave crest motion concerning the liquid film. The model approximates the wave formation process in vertical annular flow, estimating the wave height in the radial direction, neglecting the gravitational forces. The proposed expression is:

$$\Delta h_{DW} = \frac{\sqrt{2} C_W \mu_l}{(\rho_l \tau_i f_{li})^{1/2}} \tag{39}$$

being τ_i the interfacial shear stress, f_{li} the interfacial liquid friction factor and C_W is a factor that estimates the surface tension on the circulation/dissipation flow in the wave.

The interfacial liquid friction factor is calculated using the correlation originally developed by Hughmark (Berna et al., 2014):

$$\sqrt{f_{li}} = K Re_L^m \tag{40}$$

where K and m are given by.
K = 3.73, m = -0.47 for $2 < Re_L < 100$.
K = 1.962, m = -1/3 for $100 < Re_L < 1000$.
K = 0.735, m = -0.19 for $1000 < Re_L$.

While the interfacial shear stress is an expression defined by the gas core mixture properties (existence of water droplets carried by the gas phase):

$$\tau_i = \frac{f_{gi} \rho_\alpha J_\alpha^2}{(\rho_l \tau_i f_{li})^{1/2}} \tag{41}$$

expression in which all magnitudes are based on the superficial gas core mixture properties. Being ρ_α the weighted mixture density, J_α the weighted mixture superficial velocity ($J_\alpha = G_g/\rho_g + G_e/\rho_l$, where G is the mass fluxes of gas and entrained droplets) and f_{gi} the interfacial gas friction factor. This last variable is given by:

$$f_{gi} = 0.079 Re_\alpha^{-1/4} \left[1 + 24 \left(\frac{\rho_l}{\rho_g}\right)^{1/3} \frac{h_{mean}}{D}\right] \tag{42}$$

being Re_α the mixture Reynolds number defined by.

$$Re_\alpha = \frac{(G_g + G_e) D}{\mu_g} \tag{43}$$

The factor C_W was defined by Ishii and Grolmes (1975).

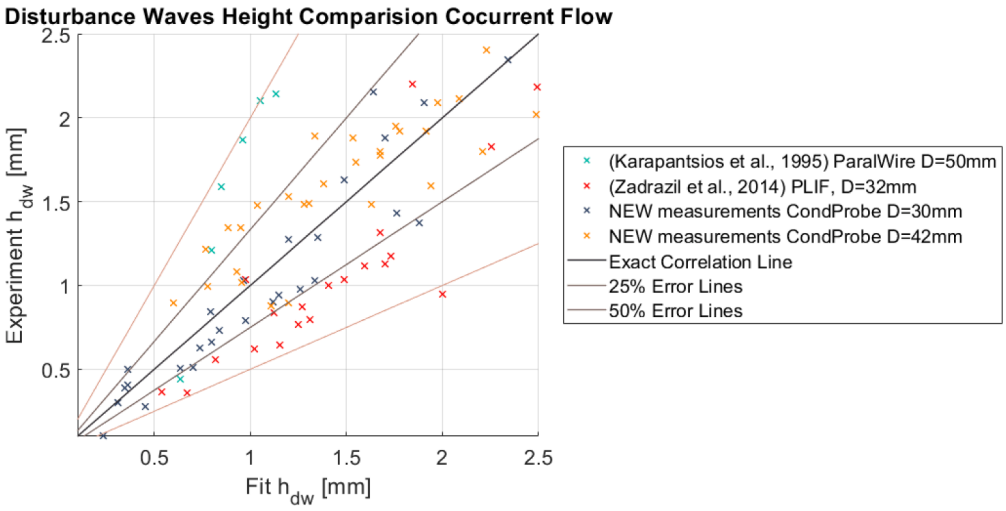

Fig. 21. Experimental data of the DWs height versus the predictions of the new correlation under Cocurrent Downward Flow conditions.

$$C_W = \begin{cases} 0.028 N_\mu for N_\mu \leq 1/15 \\ 0.25 for N_\mu > 1/15 \end{cases} \quad (44)$$

being N_μ the viscosity number, a parameter which is the ratio of viscous forces to surface tension forces and is defined as.

$$N_\mu = \frac{\mu_l}{\left(\rho_L \sigma \sqrt{\frac{\sigma}{g\Delta\rho}}\right)^{1/2}} \quad (45)$$

Han et al. (2006) carried out an experimental work under vertical upward cocurrent conditions, pipe of 9.525 mm i.d., liquid mass fluxes ranging from 126 to 198 kg/m^{2}s and gas mass fluxes ranging from 18 to 47 kg/m^{2}s. The proposed correlation is as follows.

$$\Delta h_{DW} = 4 \cdot 10^3 D Re_G^{-1.12} \quad (46)$$

Chandrasekhar developed a theoretical expression from the Kelvin-Helmholtz instability in which it is supposed that the waves are caused by the relative motion of the two continuous phases (Kolev, 2007):

$$\Delta h_{DW,K-H} = 3\pi \frac{\left(1 + \frac{\rho_g}{\rho_l}\right)\sigma_l}{\rho_g \left(u_g - u_L\right)^2} \quad (47)$$

As explained in previous sections, measurements taken at the GEPELON facility have been used to obtain a new empirical correlation, Eq. (33). Additionally, the performance of this new correlation has been tested, so several experimental data of other authors have been analysed (Fig. 21). As in the previous section, we searched for available expressions to estimate DW heights, and a reduced number of expressions have been found. The comparisons of the new correlation against the predictions for the different expressions proposed by several researchers are displayed in Fig. 22.

Fig. 22 displays the existent scattering of the reduced experimental data for the DW heights. As shown in the figure, most of the Zadrazil et al. (2014) data are fairly well predicted by the proposed correlation, while Karapantsios and Karabelas (1995) data are systematically under predicted. However, almost all the experimental data series studied are within the 50% error bands.

Fig. 22 shows the comparisons of the DW height predictions for the different expressions proposed by several researchers with those of the new expression under downward cocurrent flow conditions. As shown in the figure, there are significant differences when comparing the different expressions, particularly with Chandrasekar's expression (Kolev, 2007). This theoretical expression systematically overestimates the DWs heights for low gas Reynolds numbers. In fact, Kelvin-Helmholtz instability arises, for the case of air and water at near-atmospheric conditions, when the velocities of the working fluid differ by at least 7 m/s approximately. Han's correlation only considered the gas Reynolds number. It was developed for upward flows (Han et al., 2006), but it provides fairly accurate predictions for the configurations under study despite its simplicity and development for different flow conditions. The currently developed correlation, which gives the best results compared to the present experimental data, predicts values slightly higher than Han's expression for almost all gas and liquid Reynolds numbers.

5.2.2. *Disturbance wave frequency*

The frequency of DWs is the other variable studied in relation to the behaviour of gas–liquid interface waves. Note that the frequency shown in the following sections refers only to the DWs thus discarding the small RWs. The DWs frequency is defined as the number of waves per second and is, therefore, the inverse of the period between successive waves.

5.2.2.1. Disturbance-Wave frequency correlation. The procedure for obtaining the correlation is the same as the process followed for the DWs height. The only difference is that the frequency of the waves is obtained by means of the Strouhal number, which is the dimensionless number used to calculate the frequency. Finally, the following expression has been obtained:

$$St_l = 539 \cdot Re_L^{-0.73} \cdot \left(1 + 2.5 \cdot 10^{-3} \cdot abs\left(Re_G - Re_{G\_maxhDW}\right)^{0.56}\right) \quad (48)$$

being St_l is the Strouhal number of the liquid phase, defined as:

$$St_l = \frac{\nu_{DW} D}{J_L} \quad (49)$$

while the Reynolds numbers of the gas and liquid phases were defined in Eqs. (4) and (5).

Fig. 23 compares the experimental frequency data and the values obtained using the correlation proposed in Eq. (48). Although the scatter is slightly larger than in the previous cases, almost all the points are within the ± 30% error band. Determination coefficient R^2 obtained for this correlation is 0.805 and the RMS error is 1.35.

The trend observed for the DW frequency is different from those studied for other variables, although it shares with the DW height the particular behaviour when increasing Re_G. Generally speaking, the frequency grows as both liquid and gas Reynolds increase. However, as explained in detail in section 4.2.2, there is a slight decrease in frequency until a certain gas Reynolds number is reached, represented as Re_{G_maxhDW}. Note that the liquid Reynolds exponent is negative, which

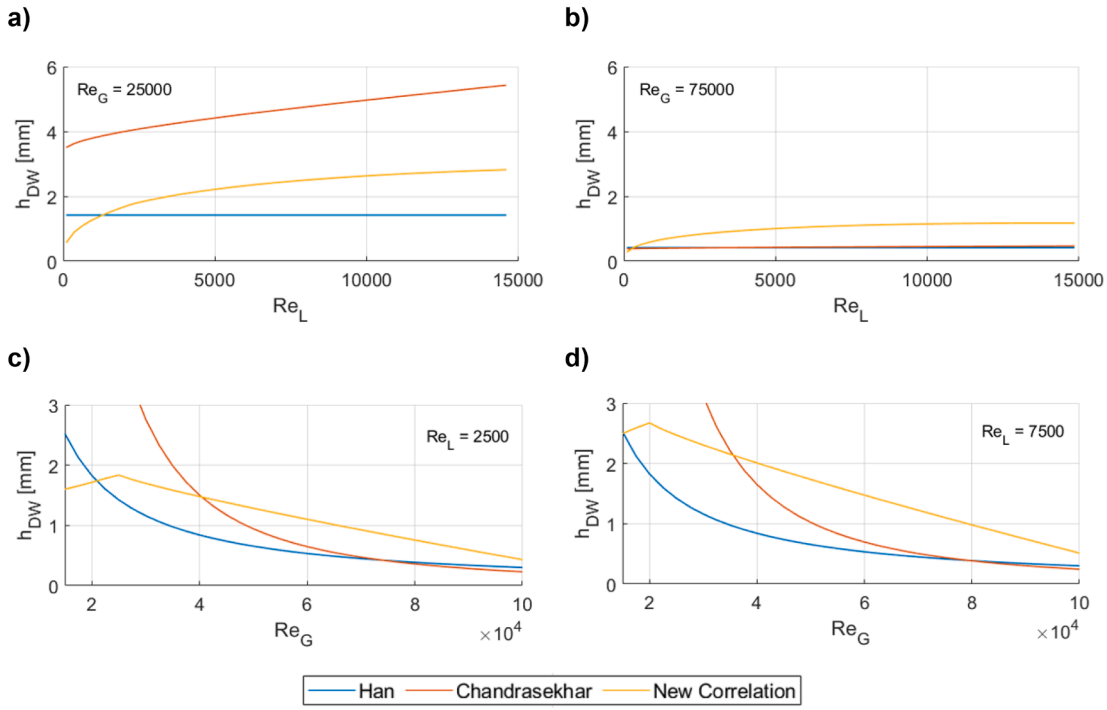

Fig. 22. Comparison of the DWs height obtained according to the empirical correlations proposed by different authors as function of: A-B) Liquid Reynolds number at constant Gas Reynolds number; C-D) Gas Reynolds number at constant Liquid Reynolds number.

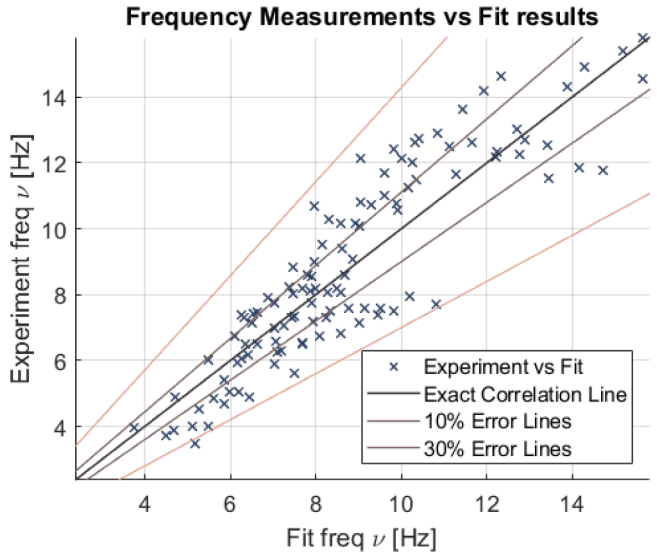

Fig. 23. Experimental DWs frequency vs. data calculated with the new correlation.

would indicate that the frequency increases as the Reynolds value decreases. However, the Strouhal number contains the liquid velocity, so if we perform a simple balance, the exponent would be + 0.27 for the superficial liquid velocity.

5.2.2.2. New correlation performance against experimental data of other authors. No expressions have been found for the DWs frequency under downstream co-current flow conditions in the literature. Although a good compendium of the DWs frequency correlations under other conditions, mainly for upward cocurrent flows, can be found in Berna et al. (2014) research. For this concerning case, as there are not available expressions for the DW frequency, only the comparison of our data against the limited number of experimental data and the performance of the newly developed correlation has been carried out, Fig. 24.

Comparing measured wave frequencies between different authors represents a challenge and can easily be misinterpreted if not done carefully. Because of the chaotic behaviour of the liquid film for different conditions and the limitations of each of the measurement systems, the interfacial waves can be presented in very different ways. Each author uses its own methods to characterise the waves, leading to different frequency measurements. In this paper, the frequency is obtained after counting the DW peaks, but other authors such as Isaenkov et al. (2020) measure the frequency as a result of adjacent pairs of peaks and crests. This leads to differences of about an order of magnitude, making the comparison of measurements very complex. Other authors use indirect methods to measure frequency, generally based on the Fast Fourier Transform (FFT), showing a frequency spectrum and, in some cases identifying the dominant one. Vasques et al. (2018) compare indirect methods such as FFT and direct counting methods obtaining errors exceeding 30%. Although the comparison may be imprecise, it has been decided to compare the experimental measurements of the authors who have estimated frequency values of large disturbance waves and have avoided counting ripple waves. However, even in this case, a large dispersion can be found caused by the differences in the criteria applied when discerning between DWs and RWs. Then, as shown in Fig. 24 and quoted above, a great dispersion exists between the experimental data of the different authors. For instance, in Takahama and Kato (1980) research, the experimental data show values of the DW frequencies much higher than those predicted by the current correlation, while Zadrazil et al. (2014) data showed a big dispersion in their measurements.

6. Conclusions

This paper shows the operation of the GEPELON installation, designed to measure the liquid film thickness in a vertical downward co-current gas–liquid flow. For this purpose, three-electrode conductance probes capable of measuring the evolution of the liquid thickness over

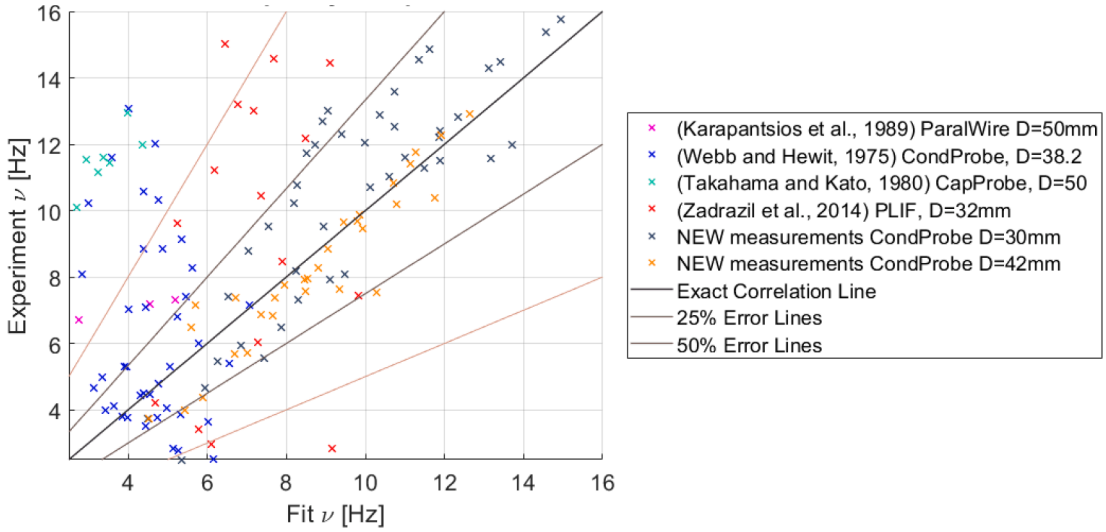

Fig. 24. Experimental data versus new correlation predictions for the Wave Frequency under Cocurrent Downward Flow conditions.

time have been designed. In addition, for these probes to work properly, it has been necessary to study and manufacture the specific port to reduce flow disturbance and the electronic circuitry to maintain a reliable and clean signal. The signal collected at a sampling rate of $5{\cdot}10^3$ samples per second is converted into distance after a calibration process specifically designed to analyse each probe individually. Six runs have been measured for each experimental condition for ten seconds each in order to analyse the random error. Furthermore, other possible sources of systematic errors, such as the calibration and adjustment process or the data acquisition system, have been studied.

Different variables related to the liquid film can be studied with the information obtained in this facility. In this paper, an in-depth analysis of the average film thickness, disturbance wave height and disturbance wave frequency has been carried out. Correlations have been proposed for each of these variables as a function of the input conditions expressed as dimensionless numbers. In addition, both the experimental measurements and the proposed correlations have been compared with research data from several authors.

It has been observed that the liquid film thickness grows as we increase the liquid Reynolds number; however, it decreases more strongly with the gas Reynolds number. The same tendencies with the gas and liquid flow rates have been observed for the height of the disturbance waves. Nevertheless, a maximum value of this variable has been measured at approximately $2{\cdot}10^4$-$4{\cdot}10^4$ gas Reynolds numbers depending on the liquid Reynolds number. This range corresponds to the change of annular flow sub-regime also observed by other authors. The influence of the gravitational force in this zone becomes less significant, being gas–liquid interaction predominant from here onwards.

For the wave frequency data, a direct proportionality for both gas and liquid flows has been observed, showing similar behaviour to the wave height. In this case, a constant or slow reduction of the wave frequency is also shown up to $2{\cdot}10^4$-$4{\cdot}10^4$ gas Reynolds numbers approximately, depending on the liquid Reynolds number. Three new correlations have been proposed for each of the three studied variables.

Regarding the mean liquid film thickness correlations, highlight that the cocurrent downward flow correlations are obtained by adding a term to the free falling correlation to consider the effect of the air stream (through the use of the gas Reynolds number). In contrast, the dependency of this variable with the distance to the flow entrance (degree of flow development) has been captured by using an exponential term in the cocurrent correlation (mean film thickness comes to a saturation value downstream depending on the gas and liquid Reynolds numbers).

We must conclude this research by summarising some important insights. It has been presented a notorious contribution of new data to the experimental database and the development of several new correlations for the most important variables of vertical downward cocurrent annular flows. There are many theoretical expressions and empirical correlations to determine the mean film thickness under free falling conditions, most of them based on Nusselt's one. However, this number is drastically reduced when downward cocurrent flows are analysed and, finally, studies and expressions to consider the degree of flow development are extremely scarce. There is also a small number of theoretical and experimental studies concerning the characteristics of the large amplitude waves (DWs), both heights and frequencies. The scarcity accentuates when correlating these two variables with the flow conditions. As an important contribution, correlations for both variables are proposed throughout this paper, and their performance has been tested against the limited experimental data available.

CRediT authorship contribution statement

Y. Rivera: Conceptualization, Methodology, Software, Formal analysis, Investigation, Writing – original draft, Writing – review & editing, Visualization. **C. Berna:** Conceptualization, Methodology, Validation, Formal analysis, Investigation, Writing – original draft, Writing – review & editing, Visualization, Supervision. **J.L. Muñoz-Cobo:** Methodology, Validation, Resources, Writing – review & editing, Supervision, Project administration, Funding acquisition. **A. Escrivá:** Validation, Resources, Writing – review & editing, Supervision, Project administration. **Y. Córdova:** Software, Investigation, Writing – review & editing.

Declaration of Competing Interest

The authors declare that they have no known competing financial interests or personal relationships that could have appeared to influence the work reported in this paper.

Acknowledgements

This research is supported by the EXMOTRANSIN project ENE2016-79489-C2-1-P included in the I + D Spanish plan. Funding for open access charge: CRUE-Universitat Politècnica de València.

References

Alekseenko, S., Antipin, V., Cherdantsev, A., Kharlamov, S., Markovich, D., 2008. Investigation of waves interaction in annular gas-liquid flow using high-speed fluorescent visualization technique. Micrograv. Sci. Technol. 20 N°1, 271.

Alekseenko, S., Cherdantsev, A., Heinz, O.M., Kharlamov, S.M., Markovich, D.M., 2009. Two-wave structure of liquid film and wave interrelation in annular gas-liquid flow with and without entrainment. Phys. Fluids 21 N°1. Ner 061701.

Alekseenko, S.V., Cherdantsev, A., Kharlamov, S., Markovich, D., 2014. Analysis of spatial and temporal evolution of disturbance waves and ripples in annular gas-liquid flow. Int. J. Multiph. Flow 67, 122–134.

Alekseenko, S.V., Cherdantsev, A.V., Cherdantsev, M.V., Isaenkov, S.V., Markovich, D. M., 2015. Study of formation and development of disturbance waves in annular gas-liquid flow. Int. J. Multiph. Flow 77, 65–75.

Aliyu, A.M., 2015. Vertical annular Gas-Liquid Two-Phase flow in Large Diameter Pipes. Cranfield University, Bedfordshire Shrivenham, Oxfordshire, England. Ph.D. Thesis.

Berna, C., Escrivá, A., Muñoz-Cobo, J.L., Herranz, L.E., 2014. Review of droplet entrainment in annular flow: interfacial waves and onset of entrainment. Prog. Nucl. Energy 74, 14–43.

Berna, C., Escrivá, A., Muñoz-Cobo, J.L., Herranz, L.E., 2015. Review of droplet entrainment in annular flow: characterization of the entrained droplets. Prog. Nucl. Energy 79, 64–86.

Bevington, P.R., Robinson, D.K., 2003. Data Reduction and Error Analysis in the Physical Sciences, Third Edition.

Brauner, N., 1987. Roll wave celerity and average film thickness in turbulent wavy film flow. Chem. Eng. Sci. 42 (2), 265–273.

Brotz, W., 1954. Uber die Vorausberedinung der Absorptions geschwineig von Gayen instromenden flussig kectsschichten. Chem Ing. Tech. 26, 470–478.

Charogiannis, A., An, J.S., Voulgaropoulos, V., Markides, C.N., 2019. Structured planar laser-induced fluorescence (S-PLIF) for the accurate identification of interfaces in mulpiphase flows. Int. J. Multiph. Flow 118, 193–204.

Cherdansev, A.V., Charogiannis, A., Markides, C.N., 2019. Simultaneous application of two laser-induced fluorescence approaches for film thickness measurements in annular gas-liquid flows. Int. J. Multiph. Flow 119, 237–258. https://doi.org/10.1016/j.ijmultiphaseflow.2019.07.013.

Chu, K.J., Dukler, A.E., 1974. Statistical characteristics of thin, wavy films: part ii. studies of the substrate and its wave structure. AIChE 20 (4), 695–706.

Chu, K.J., Dukler, A.E., 1975. Structure of the Large Waves and their Resistance to Gas-Flow. AIChE 21 (3), 583–593.

Clark, W., 2001. The Interfacial Characteristics of Falling Film Reactors. University of Nottingham, Nottingham, UK. Ph.D. Thesis.

Cuadros, J.L., Rivera, Y., Berna, C., Escrivá, A., Muñoz-Cobo, J.L., Monrós-Andreu, G., Chiva, S., 2019. Characterization of the gas-liquid interfacial waves in vertical upward co-current annular flows. Nucl. Eng. Des. 346, 112–130.

Czernek, K., Witczak, S., 2020. Precise determination of liquid layer thickness with downward annular two-phase gas-very viscous liquid flow. Energies 13, 6529. https://doi.org/10.3390/en13246529.

Dasgupta, A., Chandraker, D.K., Kshirasagar, S., Raghavendra, R.B., Rajalakshimi, R., Nayak, A.K., Walker, S.P., Vijayan, P.K., Hewitt, G.F., 2017. Experimental investigation on dominant waves in upward air-water two-phase flow in churn and annular regime. Exp. Therm Fluid Sci. 81, 147–163.

De Jong, P., Gabriel, K.S., 2003. A preliminary study of two-phase annular flow at microgravity: experimental data of film thickness. Int. J. Multiph. Flow 23, 1203–1220.

Dukler, A.E., Bergelin, O.P., 1952. Characteristics of flow in falling liquid films. Chem. Eng. Prog. 48, 557–563.

Feind, K., 1960. Stromungsuntersuchungen bei Gegenstrom von Rieselfilm und Gas in Iotrechenten Rohren. VDI Forshungsheft 26, 481–486.

Fulford, G.D., 1964. The flow of liquid in thin films. Adv. Chem. Eng. 5, 151–236.

Hall-Taylor, N.S., Hewitt, G.F., Lacey, P.M.C., 1963. The motion and frequency of large disturbance waves in annular two-phase flow of air-water mixtures. Chem. Eng. Sci. 18, 537–552.

Han, H., Zhu, Z., Gabriel, K., 2006. A study on the effect of gas flow rate on the wave characteristics in two-phase gas-liquid annular flow. Nucl. Eng. Des. 236, 2580–2588.

Hanratty, T.J., Hershman, A., 1961. Initiation of roll waves. Am. Inst. Chem. Eng. J. 7, 488.

Henstock, W.H., Hanratty, T.J., 1976. The interfacial drag and the height of the wall layer in annular flows. AIChE J. 22 (6), 990–1000.

Hewitt, G.F., Hall-Taylor, N.S., 1970. Annular Two-phase Flow. Pergamon Press, Oxford, pp. 136–139.

Holowach, M.J., Hochreiter, L.E., Cheung, F.B., 2002. A model for droplet entrainment in heated annular flow. Int. J. Heat Fluid Flow 23, 807–822.

Isaenkov, S.V., Vozhakov, I.S., Cherdansev, M.V., Arkhipov, D.G., Cherdansev, A.V., 2020. Effect of liquid viscosity and flow orientation on initial waves in annular gas-liquid flow. Appl. Sci. 10, 4366. https://doi.org/10.3390/app10124366.

Ishii, M., Grolmes, M.A., 1975. Inception criteria for droplet entrainment in two-phase concurrent film flow. AIChE J. 21, 308–318.

Karapantsios, T.D., Paras, S.V., Karabelas, A.J., 1989. Statistical characteristics of free falling films at high Reynolds numbers. Int. J. Multiph. Flow 15 (1), 1–21.

Kapitza, P.L., 1965. Collected papers of Kapitza 1938–1964. In: Ter-Harr, D. (Ed.), Wave flow of thin layers of a viscous fluid. Macmillan, New York, pp. 662–709.

Karapantsios, T.D., Karabelas, A.J., 1995. Longitudinal characteristics of wavy falling films. Int. J. Multiph. Flow 21 (1), 119–127.

Karimi, G., Kawwaji, M., 1998. An experimental study of freely falling films in a vertical tube. Chem. Eng. Sci. 53 (20), 3501–3512.

Belt, R.J., Van't Westende, J.M.C., Prasser, H.M., Portela, L.M., 2010. Time spatially resolved measurements of interfacial waves in vertical annular flow. Int. J. Multiphase Flow 36 (2010), 570–587.

Kolev N.I., "**Multiphase Flow Dynamics 2. Nuclear Thermal and Mechanical Interactions**". Springer, ISBN 978-3-540—69834-0 (2007).

Kulov, N.N., Maksimov, V.V., Maljusov, V.A., Zhavoronkov, N.M., 1979. Pressure drop, mean film thickness and entrainment in downward two-phase flow. Chem. Eng. J. 18, 183–188.

A. Leven "Filter applications", Telecommunication Circuits and Technology 2007 10.1016/b978-075065045-8/50016-x 95 160.

Liu, L., Matar, O.K., Hewitt, G.F., 2006. Laser-induced fluorescence (LIF) studies of liquid–liquid flows. Part II: flow pattern transitions at low liquid velocities in downwards flow. Chem. Eng. Sci. 61, 4022–4026.

Meza, C.E., Balakotaiah, V., 2008. Modeling and experimental studies of large amplitude waves on vertically falling films. Chem. Eng. Sci. 63, 4704–4743.

Mudawwar, I.A., El-Masri, M.A., 1986. Momentum and heat transfer across freely-falling turbulent liquid films. Int. J. Multiph. Flow 12 (5), 771–790.

Muñoz-Cobo J.L:, Chiva S., Méndez S., Monrós G., Escrivá A., Cuadros J.L., **"Development of Conductivity Sensors for Multi-Phase flow Local Measurements at the Polytechnic University of Valencia (UPV) and University Jaume I of Castellon (UJI)"**. Sensors 2017, 17, 1077; doi:10.3390/s17051077 (2017).

Muñoz-Cobo J.L:, Rivera Y., Berna C., Escrivá A., **"Analysis of conductance probes for two-phase flow and holdup applications"**. Sensors, 20, 7042; doi:10.3390/s20247042 (2020).

Nguyen, T., Balakotaiah, V., 2000. Modeling and experimental studies of wave evolution on free falling viscous films. Phys. Fluids 12 (9), 2236.

Nosoko, T., Yoshimura, P.N., Nagata, T., Oyakawa, K., 1996. Characteristics of two-dimensional waves on a falling liquid film. Chem. Eng. Sci. 51 (5), 725–732.

Nusselt, W., 1916a. Die oberflachenkondensation des wasserdampfes. Z. Vereines Dtsch Ingen. 60 (27), 541–546.

Nusselt, W., 1916b. Die oberflachenkondensation des wasserdampfes. Z. Vereines Dtsch Ingen. 60 (28), 569–575.

Padmanaban, A., 2006. Film Thickness Measurements in Falling Annular Films. University of Saskatchewan, Saskatoon, Canada. Ph.D. Thesis.

Panga, M.K.R., Mudunuri, R.R., Balakotaiah, V., 2005. Long-wave equation for vertically falling films. Phys. Rev. 71, 036310 https://doi.org/10.1103/PhysRevE.71.036310.

Rivera Y., Muñoz-Cobo J.L., Berna C., Cuadros J.L., Escrivá A., "Experimental study of the interfacial waves produced in upward vertical annular flow when varying the liquid phase surface tension". Published in the proceedings of the conference: computational and experimental methods in multiphase and complex flow X, WIT Transaction on Engineering Science, Vol 123, pp. 21-31 (2019).

Rivera Y., Muñoz-Cobo J.L., Berna C., Escrivá A., Córdova Y., **"Study of liquid film behavior in vertical downward air-water annular flow"**. Published in the proceedings of the conference: Advances in Fluid Mechanics, XIII, WIT Transaction on Engineering Science, Vol. 128, pp. 77-88 (2020).

Rivera, Y., Muñoz-Cobo, J.L., Cuadros, J.L., Berna, C., Escrivá, A., 2021. Experimental study of the effects produced by the changes of the liquid and gas superficial velocities and the surface tension on the interfacial waves and the film thickness in annular concurrent upward vertical flows. Exp. Therm Fluid Sci. 120, 110224.

Schubring, D., Shedd, T.A., 2008. Wave behavior in horizontal annular air-water flow. Int. J. Multiphase Flow 34, 636–646.

Rodriguez, D.J., Shedd, T.A., 2004. Entrainment of gas in the liquid film of horizontal, annular, two-phase flow. Int. J. Multiphase Flow 30 (6), 565–583. https://doi.org/10.1016/j.ijmultiphaseflow.2004.04.011.

Schubring, D., Ashwood, A.C., Shedd, T.A., Hurlburdt, E.T., 2010. Planar laser-induced fluorescence (PLIF) measurements of liquid film thickness in annular flow. Part I: Methods and data. Int. J. Multiph. Flow 36, 815–824.

Setyawan, A., Indarto, I., Deendarlianto, A., 2016. The effect of the fluid properties on the wave velocity and wave frequency of gas-liquid annular two-phase flow in a horizontal pipe. Exp. Therm Fluid Sci. 71, 25–41.

Takahama H., Kato, S., **"Longitudinal flow characteristics of vertically falling liquid films without concurrent gas flow"**. International Journal of Multiphase Flow, Vol. 6, No 3, pp. 203–215(1980).

Telles, A.S., Dukler, A.E., 1970. Statistical characteristics of thin, vertical, wavy, liquid films. Ind. Eng. Chem. Fundam. 9 (3), 412–421.

Tiwari, R., Damsohn, M., Prasser, H.M., Wymann, D., Gossweiler, C., 2014. Multi-range sensors for the measurement of liquid film thickness distributions based on electrical conductance. Flow Meas. Instrum. 40, 124–132.

Vasques, J., Cherdansev, A., Cherdansev, M., Isaenkov, S., Hann, D., 2018. Comparison of disturbance wave parameters with flow orientation in vertical annular gas-liquid flows in a small pipe. Exp. Therm Fluid Sci. 97, 484–501.

Wallis, G.B., 1969. One-Dimensional Two-Phase Flow. McGraw-Hill Inc, New York, USA.

Webb, D.R., Hewitt, G.F., 1975. Downwards co-current annular flow. Int. J. Multiph. Flow 2, 35–49.

Wolf A., "**Film structure of vertical annular flow**". PhD. Thesis University of London University and Diploma of Membership of Imperial College (1995).

Wolf, A., Jayanti, S., Hewitt, G.F., 2001. Flow development vertical annular flow. Chem. Eng. Sci. 56, 3221–3225.

Zadrazil, I., Matar, O.K., Markides, C.N., 2014. An experimental characterization of downwards gas-liquid annular flow by laser-induced fluorescence: Flow regimes and film statistics. Int. J. Multiph. Flow 60, 87–102.

Zhao, Y., Markides, C.N., Matar, O.K., Hewitt, G.H., 2013. Disturbance wave development in two-phase gas–liquid upwards vertical annular flow. Int. J. Multiph. Flow 55, 111–129.